Revision 1

Berthierine-like mineral formation and stability during the interaction of kaolinite with metallic iron at 90°C under anoxic and oxic conditions.

Camille Rivard[1,2], Manuel Pelletier[1,2], Nicolas Michau[3], Angelina Razafitianamaharavo[1,2], Isabelle Bihannic[1,2], Mustapha Abdelmoula[4,5], Jaafar Ghanbaja[6] and Frédéric Villiéras[1,2]

[1] Université de Lorraine, LEM, UMR7569, Vandœuvre-lès-Nancy, F-54500, France

[2] CNRS, LEM, UMR7569, Vandœuvre-lès-Nancy, F-54500, France

[3]ANDRA, 1/7 rue Jean Monnet, Parc de la Croix Blanche, 92298 Châtenay-Malabry Cedex, France

[4] Université de Lorraine, LCPME, UMR7564, Vandœuvre-lès-Nancy, F-54500, France

[5] CNRS, LCPME, UMR7564, Vandœuvre-lès-Nancy, F-54500, France

[6] Université de Lorraine, SCMEM, Vandœuvre-lès-Nancy, F-54500, France

Abstract: The interaction between metallic iron and kaolinite was studied in conditions relevant to those that may be encountered in a high-level radioactive waste disposal facility in geological formation. Experiments were carried out under anoxic atmosphere at 90°C and in chloride solutions to simulate conditions close to disposal facilities. KGa-2 kaolinite was put in contact with powdered metallic iron in batch experiments for durations of 1, 3 and 9 months. Solutions extracted from the end-products were analyzed (pH, Eh, conductivity and cations concentrations). End-products were characterized by a set of chemical (oxides analyses, CEC, EDXS) and mineralogical techniques (SEM, TEM, XRD and FTIR), textural analyses (nitrogen adsorption and low-pressure argon adsorption), XPS and Mössbauer spectroscopy. In another set of experiments the system was changed from anoxic to oxic conditions to evaluate the stability of the system in the presence of O_2.

The interaction between metallic iron and kaolinite led to a fast initial reaction as major modifications took place during the first month. The partial oxidation of metallic iron resulted

in a pH increase and negative Eh values. Iron was not found in solution but in two new Fe-rich phases: magnetite in very low amounts and a Fe-rich clay phase, belonging to the berthierine family. Si and Al of the berthierine are derived from the partial alkaline dissolution of kaolinite, mostly along edge faces. TEM-EDXS local analyses showed that the composition of resulting particles consisted in mixtures of berthierine and kaolinite layers. Clay particles became thicker with the epitaxial growth of berthierine layers on the basal surfaces of pristine kaolinite.

Neoformed berthierine was not stable in the presence of O_2 at 90°C. Berthierine layers dissolved, iron was mobilised to form iron oxides and oxyhydroxides while kaolinite layers recrystallised from released Al and Si.

Keywords: kaolinite, metallic iron, Fe-rich serpentine, berthierine, stability.

1. INTRODUCTION

In the context of the underground disposal of High-Level radioactive Waste (HLW), Andra (French national radioactive waste management agency) has selected the Callovo-Oxfordian (COx) clay stone from Bure, France, as a potential host-rock. This rock contains quartz, carbonates (calcite and dolomite), feldspars, pyrite and 30 to 60% of clay minerals: illite, illite-smectite mixed layers, chlorite and kaolinite (Gaucher et al. 2004; Rousset 2002; Sammartino 2001; Brégoin 2003; Claret et al. 2004; Yven et al. 2007). In conditions where HLW could be stored, clay materials present in the rock are expected to evolve significantly due to the temperature generated by HLW radioactive decay, variations in water activity and the presence of engineered barrier materials such as concrete, glass and steel (Landais 2006). It is then of prime importance to understand the interaction mechanisms between Callovo-Oxfordian host-rock and iron.

Previous investigations on mineralogical transformations of COx rock in contact with powdered metallic iron or iron foils performed in batch systems have shown that the clay minerals involved in corrosion processes are mainly the illites and the mixed layers illite/smectite minerals (de Combarieu et al. 2007). Schlegel et al. (2008) analyzed the effect of iron corrosion by placing a heated iron rod in direct contact with COx rock. They observed the formation of a corrosion layer composed of two parts: a first layer corresponding to magnetite and a second layer formed with a Fe-phyllosilicate and a Ca-rich siderite. To go further into the mechanisms and to assess the role played by each clay phase, other studies have used mono-mineral samples and analyzed in detail their reactivity towards iron. Most of these studies were focused on smectites (Habert 2000; Guillaume et al. 2003, 2004; Perronnet et al. 2007; Lantenois et al. 2005; Mösser-Ruck et al. 2010; Osacky et al. 2010; Savage et al. 2010) and have shown that, at 80°C in NaCl-$CaCl_2$ solution, smectite layers destabilization was accompanied by the neo-formation of Fe-rich serpentine like-species (berthierine, odinite or cronstedtite). In comparison, fewer studies have been devoted to kaolinite. In the case of

kaolinite-smectite mixtures contacted with metallic iron at 80°C, Kohler (2001) reported the formation of a 1:1 phyllosilicate with low Fe content, while preliminary investigations on pure kaolinite (Perronnet 2004) suggested a formation of Fe-rich-serpentines (cronstedtite and berthierine). It then appears that kaolinite reactivity towards iron should be investigated in more detail to provide a complete picture of the reactivity of COx clay stone.

The present study therefore focuses on the interaction between pure kaolinite and metallic iron. Kaolinite was contacted with pure iron powder at 90°C under nitrogen atmosphere in chloride solution, i.e. in conditions relevant to those of a radioactive waste disposal facility. In a second set of experiments, air was gradually introduced into the system to assess the effect of oxygen on berthierine-like phase stability at 90°C.The resulting liquid phases were analyzed in terms of pH, Eh, conductivity and chemical composition. Solid end-products were characterized chemically (oxides analyses, cations exchange capacity, energy dispersive X-ray spectroscopy coupled to transmission electron microscopy (TEM)), mineralogically (X-ray diffraction (XRD), Fourier transformed infrared spectroscopy (FTIR), TEM, scanning electron microscopy (SEM) and X-ray photoelectron spectroscopy (XPS)) and texturally (nitrogen adsorption and low pressure argon adsorption). Further information on iron location and status in the neo-formed products was obtained by Mössbauer spectroscopy.

2. MATERIALS AND METHODS

2.1. Starting material

Georgia kaolinite (KGa-2) was supplied by the Source Clay Repository. It is a nearly pure kaolinite material with low amounts of impurities (3% of anatase and 1% of crandallite and mica and/or illite according to Chipera and Bish 2001). On the basis of TEM-EDXS analyses, Mermut and Cano (2001) proposed an average structural formula written as $(Si_{3,84}Al_{0,16})(Al_{3,80}Ti_{0,13}Fe^{3+}_{0,07})\ Ca_{0,005}Na_{0,01}K_{0,002}\ O_{10}(OH)_8$. The Cation Exchange Capacity measured by the ammonia-electrode method is 3.7 ± 0.1 meq/100 g (Borden and Giese 2001). The Specific Surface Area (SSA) of Na-saturated KGa-2, determined from application of the

Brunauer-Emmet-Teller (BET) method to nitrogen adsorption data, is of 22 +/-1 m^2/g (Hassan et al. 2005, Sayed-Hassan et al. 2006). By combining low-pressure argon adsorption experiments and atomic force microscopy measurements, the average basal length and thickness of particles were determined to be 550 nm and 40 nm, respectively.

Powdered metallic iron (α-Fe), with a 99.5 % minimum purity and an average grain size of 40 μm, was provided by Aldrich®. Its SSA (N_2 adsorption) is 0.13 ± 0.1 m^2/g.

In agreement with previous studies (Mösser-Ruck et al. 2010; Guillaume 2002; Guillaume et al. 2003, 2004) the composition of chloride solution used in the present study (NaCl: 0.0207 $mol.kg^{-1}$, $CaCl_2$: 0.0038 $mol.kg^{-1}$) was chosen to match that of natural water from the COx formation.

2.2. Experiments

The iron:clay mass ratio was fixed at 1:3. Such a value is in the range of the reactivity threshold of between 1:15 and 1:7.5 defined by Perronnet (2004) for bentonite at 80°C, which ensures sensitivity on metallic iron corrosion and clay alteration. The solution:clay ratio was fixed at 20:1. Such a value provides usable equilibrium solution volumes and is close to those used in previous iron:clay interaction experiments (16.7 in Habert 2000, Lantenois et al. 2005 and Perronnet et al. 2004, 14 in Kohler 2001 and 10 in Guillaume et al. 2004). Experiments were carried out at a fixed temperature of 90°C in order to be close to the highest temperature expected in the repository and to slightly enhance kinetics.

Before use, kaolinite powder was stored overnight in an oven at 80°C. Oxygen was removed from the solution by bubbling N_2 throughout the solution for one hour. Samples were conditioned in a MBraun Labstar glove box, under N2 atmosphere (O_2 and H_2O < 1 ppm). Kaolinite (6 g), metallic iron (2 g) and solution (120 mL) were introduced in Parr® autoclaves for anoxic experiments.

For experiments with oxygen present, polypropylene bottles (Nalgene®) were used. Due to polymer degradation resulting from high H_2 and H_2O pressures and probable thermolysis

(developed from heating and H_2 production with metallic iron oxidation), the system becomes slightly porous and O_2 can diffuse into the reactor while other gases such as H_2 and H_2O can diffuse outside. As such behaviour is important only after three months, it provides a convenient way for studying the stability of the formed end-products under oxidizing conditions.

Experiments were run for one, three and nine months. The resulting samples will be referred to as K-1m-Fe, K-3m-Fe and K-9m-Fe for anoxic experiments and as K-1m-Fe-O_2, K-3m-Fe-O_2 and K-9m-Fe-O_2 for experiments with oxygen. Blank experiments without iron were used as control (K-1m, K-3m and K-9m). A final set of experiments was carried out without any clay to observe iron corrosion in NaCl-$CaCl_2$ solution in both oxic and anoxic conditions (Fe-1.2m, Fe-3m and Fe-9m).

At the end, reactors were quickly cooled down and opened under N_2 atmosphere. Solid and liquid phases were separated by centrifugation (46,000 g during 45 min). Solutions were filtered at 0.2 µm, acidified by nitric or hydrochloric acid and frozen. Solid fractions were frozen, freeze-dried then gently ground to powder in an agate mortar. Solid samples were stored under anoxic atmosphere. The time spent under oxygen atmosphere due to samples preparation was minimized before characterization.

2.3. End-products characterization

2.3.1. Liquid phase characterization

pH and Eh measurements of the supernatants were carried out under anoxic atmosphere at room temperature using an Ag/AgCl pH electrode (VWR) and a Sentix®ORP electrode (WTW). Initial state was measured on a clay-experimental solution mixture, in identical proportions to the reactive systems. The chemical composition of the solutions (initial and experimental) was measured by ICP-OES (Si, Al, Fe_{tot}, Mn, Mg, Ca and K) on HNO_3 acidified supernatants. The amount in Fe^{2+} cations was measured by colorimetry on a parallel aliquot (HCl acidified).

2.3.2. Solid phase characterization

Cation Exchange Capacity was measured after exchange with cobaltihexamine ($Co(NH_3)_6Cl_3$) and dosage of its residual concentration in the equilibrium solution (Mantin 1969; Mantin and Glaeser 1960; Morel 1957). 1.5 g of sample was dispersed and shaken during two hours at 30°C in 30 mL of cobaltihexamine solution ($16{,}6.10^{-3}$ mol/L). Samples were then centrifuged for one hour at 46,000 g. Supernatants were analyzed on a Shimadzu UV-2501PC spectrophotometer, using cobaltihexamine ion absorption band at 472 nm to derive CEC from residual concentration in cobaltihexamine ($CEC_{A472\text{-}Co}$). Concentrations in Na, K, Ca, Mg, Fe, Al and Si in supernatants were measured by atomic absorption, using a Perkin Elmer AA800 set-up, to calculate CEC from exchanged cations (CEC_{Cat}). Measurements were always carried out in duplicate to check for reproducibility.

Contents of Na, K, Ca, Mg, Fe and Al in solid end-products were measured by atomic absorption on a Perkin Elmer AA800 set-up after fusion of 200 mg of sample in $LiBO_2$ (1 g) at 1,000°C and dissolution in 100 mL of hydrochloric acid (1 N). Silicon concentration was determined by spectrophotometry (band at 850 nm) after formation and reduction of the yellow silico-molybdic $Si(Mo_{12}O_{40})$ complex. Loss on ignition of each sample was obtained using 2 g of initial kaolinite or 0.7 g of end-products heated at 1,060°C for two hours.

For the SEM analysis of coarse fractions, the bulk sample was subjected to successive ultrasonic treatments and sedimentation in alcohol until a particle-free supernatant was obtained. Remaining grains were dried under nitrogen atmosphere, placed on carbon adhesive sticks and carbon coated. Scanning electron micrographs were obtained using a Hitachi FEG S-4800. The energy dispersive X-ray spectrometer was also used to obtain semi-quantitative chemical analyses coupled to SEM images.

For the TEM analysis of fine fractions, 10 milligrams of powder were dispersed in ethanol and treated ultrasonically for 5 min. One drop of the suspension was placed on a carbon coated copper grid and evaporated. TEM micrographs and Selected Area Electron Diffraction

(SAED) were carried out using a CM20 Philips microscope running at 200 kV. Chemical compositions were determined using energy dispersive X-Ray spectroscopy (EDXS). EDX spectra were recorded by means of an PGT (Princeton Gamma Tech) spectrometer equipped with an ultrathin window (Si-Li) X-Ray detector. The analysis was carried out in nanoprobe mode with a diameter of the probe of 10 nm. For each reacted sample, at least 20 analytical points were recorded on isolated particles. Counting time was about 40 s with a dead time between 10 and 50 %. To avoid any artifacts due to the presence of remaining chlorides, all spectra displaying chlorine species were not included in the analyses. High-Resolution TEM images were also carried out by embedding samples in an organic polymer (Epon 812) and subsequent ultramicrotoming ultrathin sections (thickness of 50 to 90 nm). The obtained slices were placed on a carbon coated copper grid and observed at high magnification (x 200,000).

Nitrogen adsorption-desorption isotherms at 77 K were recorded on a step-by-step automatic set-up built in the Laboratoire Environnement et Minéralurgie (LEM). Prior to adsorption experiments, samples were outgassed at 110°C during 18 hours under a residual vacuum of 0.01 Pa. Specific Surface Areas (SSA) were determined from the Brunauer-Emmet-Teller (BET) equation (Brunauer et al. 1938) using 16.3 Å as the cross-sectional area of nitrogen molecules.

Low-pressure isotherms at 77 K were recorded on a lab-built automatic quasi-equilibrium volumetric set-up (Villiéras et al. 1992, 1997b; Michot et al. 1990). High-purity argon (>99.995 %) was provided by Air Liquide (Alphagaz Ar2). Around 1.5 g of sample was outgassed overnight at 110°C under a residual pressure of 10^{-4} Pa. After outgassing, a slow, constant and continuous flow of argon was introduced into the adsorption cell through a micro leak. As the introduction rate is low, the measured pressures can be considered as quasi-equilibrium pressures (Michot et al. 1990; Villiéras et al. 1997a). High-resolution adsorption isotherms with more than 2,000 data points describing the filling of the first monolayer were

obtained by recording quasi-equilibrium pressure as a function of time. Due to the large number of experimental data points, the experimental derivative of the adsorbed quantity can be calculated as a function of the logarithm of relative pressure, $\ln(P/P_0)$, which corresponds to the free energy of adsorption expressed in kT or RT (Villiéras et al. 1992, 1997a; b). The derivative adsorption isotherm can then be considered as a fingerprint of the adsorption energy distribution for the gaseous probe. Experimental data were further analysed using the Derivative Isotherm Summation (DIS) procedure (Villiéras et al. 1992; 1997a; b; 2002) and the modelling strategy proposed by Hassan et al. (2005) for kaolinite to estimate Ar specific surface areas, their distribution between basal and edge surface areas and to derive mean length and thickness of clay particles.

Bulk samples were analyzed by XRD using 1 g of randomly oriented powder, put on a rotating sample holder and leveled with a glass slice to obtain a flat surface. XRD data were also acquired using zincite (ZnO) as an internal standard. In this latter case, samples were first mixed with 0.111 g of ZnO and ground in an agate mortar for 5 min. XRD patterns were collected on a D8 Advance Bruker AXS diffractometer equipped with a LynxEye fast linear detector using Cobalt Kα radiation (λ=0.17903 nm) at 35 kV and 45 mA. Intensities were recorded from 3 to 64°2θ with a 0.035°2θ step using a 3 s counting time per step. In the presence of the standard, intensities were recorded from 4 to 80°2θ with a 0.02°2θ step using a 3 s counting time per step. Data reduction and analysis were performed with the *EVA* software (*DIFFRACplus* from Bruker) and diffraction peaks were identified by comparison with powder diffraction files (PDF2 database from the International Center for Diffraction Data, ICDD).

FTIR spectra were collected on bulk powder samples mixed with KBr as a transparent matrix. Diffuse reflectance FTIR spectra were recorded on a Bruker IFS-55 spectrometer in the range from 4,000 to 600 cm^{-1} with a resolution of 2 cm^{-1}. Spectra were obtained from the average of 200 scans collected during 2 min. Data reduction and analysis were performed using the

OPUS program (from Bruker). Specific bands of atmospheric water vapor and CO_2 were removed from the spectra; bands attribution was done on the basis of reference works (Farmer 1974; Van der Marel and Beutelspacher 1976; Russell and Fraser 1994).

^{57}Fe Mössbauer spectroscopy was used to accurately determine iron oxidation states and their location in the different phases (oxides, hydroxides, clays…). Bulk powder samples were placed on a sample holder under He atmosphere and then quickly placed in the cryostat at high vacuum (10^{-6} mBar). Transmission Mössbauer spectra were collected using a 50 mCi source of ^{57}Co in rhodium. Spectrometer calibration was performed using a 25 µm foil of α-Fe at room temperature. Spectra were acquired at room temperature (295 K) and spectra adjustments were performed using Lorentzian-shape lines.

XPS spectra were obtained using a KRATOS Axis Ultra X-ray photoelectron spectrometer with a monochromatized Al Kα X-ray source (λ = 1486.6 eV) operated at 150 W. The samples were pressed onto a Cu tape on a holder and introduced into the spectrometer. The base pressure in the analytical chamber was ≈10^{-9} mbar. Spectra were collected at normal (90°) take-off angle. Survey scans were used to determine the chemical elements at the clay surface. They were acquired with a pass energy of 160 eV and a X-ray spot size of 0.3 mm x 0.7 mm. Narrow region photoelectron spectra were used to determine chemical state information. They were acquired with an analyzer pass energy of 20 eV and an X-ray spot size of 0.3 mm x 0.7 mm. The binding energy was calibrated by assigning the C(1 s) peak of contamination carbon to 284.6 eV. Spectra for Fe, O, Si and Al were fitted using a Shirley Background and a pseudo-Voigt peak model.

3. RESULTS

3.1. Iron oxidation in the absence of clay

Reaction products of iron in the absence of clay were black and brown for anoxic and oxic conditions, respectively.

248 *3.1.1. Liquid phase analyses*

249 After reaction in anoxic atmosphere, the pH was higher than in the initial state and reached
250 values around 9 whatever reaction time (Fig. 1a and Table 1). The initial Eh was negative and
251 decreased drastically after reaction from –115 to –386 mV (Fig.1b and Table 1). In Fe-1m
252 sample conductivity was higher than in the initial state but decreased with time. In the
253 presence of O_2, pH values were lower than both initial and anoxic values and increased
254 slightly with time. Whatever the time, Eh is positive, indicating oxidising conditions.
255 Cation concentrations in the initial solution (contacted with metallic iron during 24 h)
256 revealed low Fe content (0.68 mg/L) as well as small amounts of K and Mg (Table 1). These
257 latter impurities may have been present either in solution or at the surface of iron grains. In
258 Fe-1m the concentration in iron has significantly decreased down to 0.08 mg/L indicating that
259 iron is not stable in such solutions and that an iron-bearing phase precipitates. In Fe-3m and
260 Fe-9m, Fe concentrations remain very low. In contrast, in the presence of O_2, higher Fe
261 concentrations (measured only after 10 months) were measured. Such values are partly due to
262 a decrease in water amount resulting from water vapour diffusion from the reactor. This is
263 confirmed by the significant increase in both Na and Ca concentrations and conductivity.
264 Using the former value, an evaporation percentage of 66 to 70% can be estimated. The water
265 mass required for a complete corrosion of metallic iron can be estimated at 0.64 g a much
266 lower value than that due to evaporation. The corrected iron concentration can then be
267 estimated at around 1.2 to 1.4 mg/L, i.e, a value significantly higher than in the absence of O_2,
268 but still rather low.

269 *3.1.2. Solid phase analyses*

270 In the absence of O_2 and whatever the reaction time, corrosion products are magnetite
271 agglomerates of less than 100 μm (Fig. 2a). SEM studies reveal crystals of various sizes
272 developing around pristine metallic iron grains. For Fe-1m and Fe-9m samples, the maximal
273 thickness of magnetite growing around metallic iron grains is 10 μm.

Powder XRD confirmed the presence of both metallic iron and magnetite in Fe-1m, Fe-3m and Fe-9m. In quantitative terms, the decrease in metallic iron is important during the first month (49% of iron consumed in Fe-1m) and slows down after (56% of iron in Fe-9m). Reaction products are not stable at ambient atmosphere as after 24 h, FeO was formed from oxidation of metallic iron.

The reaction is much more advanced in the presence of O_2 as metallic iron is totally oxidized for Fe-1m-O_2. Magnetite is present as in the former case, but other oxides (hematite, Fe_2O_3) are found together with oxyhydroxides (goethite, FeOOH), which confirms oxidizing conditions. At longer times (Fe-3m-O_2), maghemite (γ-Fe_2O_3) appears while the amount of hematite increases, at the expense of magnetite.

3.2. Evolution during the interaction of kaolinite with metallic iron

Whatever the time, solid end-products were observed at the bottom of the Teflon-liner with clear supernatants. Whereas the initial kaolinite and the kaolinite reacted in the absence of iron were almost white, all end-products under anoxic atmosphere displayed a dark-green colour, suggesting the presence of mixture of ferrous and ferric iron. K-1m-Fe-O_2 sample was green as K-1m-Fe, whereas after 3 months of reaction, the colour progressively changed to red, indicating an oxidation of the end-products.

3.2.1. Solution chemistry

In the absence of iron, the pH and Eh values remain constant (Fig. 1c and d). The situation is markedly different in the presence of iron. Indeed a strong increase in pH to a value around 8.5 is observed during the first month with stabilization between 1 and 9 months under anoxic atmosphere (Table 1). Similarly, the Eh evolves strongly from positive to negative in the first month and remains rather constant thereafter. Differences in conductivity between the two experiments are more marginal although experiments in the presence of iron display a slightly lower conductivity. In the experiments allowing O_2 diffusion into the reactors, pH and Eh values of K-1m-Fe-O_2 are rather similar than those of K-1m-Fe but the values strongly

300 diverge for longer times with lower pH and higher Eh and conductivity. The pH and Eh
301 values of K-9m-Fe-O_2 are close to those obtained in the absence of iron. Conductivity
302 increases in relation with water loss.
303 Under anoxic conditions, chemical analyses of the solutions (Table 1) reveal only small
304 differences due to the presence of iron in contact with kaolinite. The main difference lies in
305 the amount of Mg that is significantly lower in the presence of iron, indicating that this
306 element is likely remobilized in solid phases when iron is present. The amount of Fe^{2+} after
307 reaction with iron is even lower than in absence of metallic iron. In the presence of O_2, the
308 concentrations are close to those obtained without O_2, except for Mg that is present in K-3m-
309 Fe-O_2 and K-9m-Fe-O_2 whereas it was not detected in the anoxic experiments.

310 *3.2.2. Cation Exchange Capacity*
311 Initial CEC values were calculated for both raw kaolinite and kaolinite equilibrated with
312 chloride solution at ambient temperature to take into account the perturbation due to the
313 chloride solution (Table 2). Indeed, initial KGa-2 is Na-K-Ca-Mg equilibrated whereas it is
314 only Na-Ca equilibrated after exchange with the solution, Mg and K being transferred to the
315 solution, as revealed by their presence in solution (Table 1). K and Mg are thus negligible at
316 the surface of the kaolinite after exchange with solution. CEC_{Cat} (4.0 meq/100 g) is
317 significantly higher in the equilibrated kaolinite and is higher than $CEC_{A472\text{-}Co}$
318 (2.1 meq/100 g). This is due to Ca and Na cations from interstitial solution that remain after
319 centrifugation. Still, the ratio Na:Ca is significantly lower than that of the chloride solution
320 showing a preferential adsorption of Ca^{2+}. Initial CEC values in the presence of iron were
321 calculated by considering metallic iron CEC value as negligible. In the presence of iron
322 $CEC_{A472\text{-}Co}$ values are much higher than CEC_{Cat}. As we had evidenced this difference is due to
323 an interference with metallic iron (Rivard et al., in preparation), only CEC_{Cat} values are
324 considered in the following.

In the absence of iron, very little evolution of cations concentrations is observed, except for dissolved Al that is not detected any more after the reaction. In the presence of iron, the values are lower than in the absence due to dilution. Compared with the case in the absence of iron, concentrations obtained on samples after reaction under anoxic atmosphere exhibit an increase in Na and a decrease in Ca, Al and Mg, with nearly no evolution between 1 and 9 months. It must be pointed out that no exchangeable Fe is observed, which, combined with solution results, shows that all Fe is fixed in solid phases. Furthermore, CEC measurements reveal the full consumption of Mg and Al and the partial one of K and Ca, all these elements being likely retained in solid phases. In contrast Na is not consumed and becomes the main surface cation for the phases present after reaction.

CEC_{Cat} value of K-1m-Fe-O_2 is roughly similar to the value of K-1m-Fe (3.0 and 2.8 meq/100 g respectively). After three months of reaction, an increase of the CEC is observed in comparison to values obtained after one month of reaction, with values of 4.0 and 4.7 meq/100 g for K-3m-Fe-O_2 and K-9m-Fe-O_2, respectively. The cations distribution showed an increase of all the elements (except Al, not detected as usual) in comparison with experiments in the absence of O_2. This increase could be attributed to the concentration of elements in the interstitial solution due to water loss.

3.2.3. Morphological changes

Whereas blank experiments SEM and TEM observations do not reveal any significant changes (not shown), materials reacted with iron show significant morphological modifications. In the coarse fractions, large (10 to 100 μm) and well-crystallized magnetite particles are observed together with nodules of partially transformed clay particles sometimes associated with small magnetite crystals (example with K-1m-Fe in Fig. 2b). In these nodules, the initial hexagonal shape of pristine kaolinite is lost and the eroded edges are apparent. In K-9m-Fe, new phyllosilicates with an alveolar shape are also observed (Fig. 2c). Metallic iron grains are only visible on ultra-thin cuttings of resin embedded coarse fraction (Fig. 2d).

Residual metallic iron appears coated with a thin layer of iron-rich clay particles (thickness less than 3 μm). At the interface between iron and clays, small iron oxides particles (0.5 to 2 μm) are also observed. On certain aggregates of K-9m-Fe sample, metallic iron has totally disappeared and their initial presence is revealed by cavities surrounded by magnetite and Fe-rich clay halos (Fig. 2e). In the presence of O_2, similar features as those revealed in the absence of O_2 were observed, except for K-9m-Fe-O_2 sample where the number of iron metallic grains coated by clay agglomerates appears to decrease.

TEM observations of the fine fractions clearly show the above-mentioned shape changes (Fig. 4). Kaolinite particles lose their hexagonal shape and eroded edges appear. Such an evolution is more marked with increasing reaction time, which suggests that the neoformed crystals are far from their equilibrium shape. With O_2 entrance small magnetite crystals (from 20 to 500 nm) were observed associated with eroded clay particles or in the vicinity of particles (arrow on Fig. 4d) whatever the reaction time. However, the K-9m-Fe-O_2 sample presents globular clusters that can be identified as maghemite by combining EDXS analyses and SAED (arrows on Fig. 4e).

Fig. 5 presents the N_2 adsorption-desorption isotherms obtained after reaction in the presence and in the absence of iron. For experiments under anoxic atmosphere, both isotherms are almost superimposed to the pristine kaolinite one and display a very small hysteresis between adsorption and desorption. The initial SSA of kaolinite is 20.5 ± 1 m^2/g a value close to that determined by Sayed Hassan et al. (2006) (22 +/-1 m^2/g). As the SSA of metallic iron is negligible, the theoretical initial SSA of the mixture corresponds to 75 % of that of initial kaolinite SSA, i.e. 15.4 m^2/g. No significant evolution of SSA is observed in blank experiments (Fig. 5b; Table 3). After one month reaction with iron, the SSA increases from 15.4 to about 18 m^2/g and remains stable thereafter. In the presence of O_2, while the shape of the isotherms remains the same, a significant increase in adsorbed amount is observed for K-3m-Fe-O_2 and K-9m-Fe-O_2 samples in comparison with anoxic experiments and K-1m-Fe-O_2.

In agreement with the isotherms, the SSAs of the initial, K-9m, K-9m-Fe and K-1m-Fe-O_2 are very close (20.5, 21.1, 17.7 and 20.5 m^2/g, respectively). In contrast, the isotherms obtained for the products reacted for longer times display a significant increase in SSA to values of 34 and 53 m^2/g for K-3m-Fe-O_2 and K-9m-Fe-O_2, respectively (Table 3).

Low-pressure argon adsorption isotherms were measured for all Fe-reacted samples and were compared to the K-1m sample. This latter choice is related to the surface cation composition which, as shown by Hassan et al. (2005), influences adsorption isotherm profiles. Derivative argon adsorption isotherms (Fig. 6a) display features typical of phyllosilicates. According to Villiéras et al. 1992, the major peak at medium-energy (around –4.5 $\ln(P/P_0)$) corresponds to adsorption on basal faces whereas the high energy tail can be assigned to adsorption on edges faces. After the first month of reaction with iron, the peak corresponding to adsorption on basal faces has lost intensity and is shifted towards higher energy (–4.35 instead of –4.10 initially). No further modification occurs with increasing reaction time. Considering the DIS-method, seven local derivatives are needed for a proper fit of experimental derivative (Fig. 6a; Annex 1). This is one more domain than the decomposition shown by Sayed-Hassan et al. (2006). This difference can be tentatively assigned to the bi-ionic nature of surface species in our case compared to the monoionic case studied by Sayed-Hassan et al. (2006). The presence of iron shifts the position of domain 5 towards lower energy and that of domain 6 towards higher energy. Domain 4, around -5.7, exhibits an increase in lateral interaction with time, a feature that suggests that this domain becomes more homogeneous upon reaction with iron. Mean particle sizes were calculated from basal and edge SSAs derived from DIS analyses. Initial particles have a mean length of 472 nm and a mean thickness of 47 nm, values that are close to those already obtained for Na-saturated KGa-2 by Sayed-Hassan (2005). In the presence of iron, basal surface areas decrease of about -30 %, whereas edge surface areas increase (+77 %). This induces a significant modification of particles geometry with a decrease in width (-40 % in K-9m-Fe) and an increase in thickness (around +30 %).

403 Consequently, the mean number of 7 Å layer per particles increases from 65 to 95 after
404 reaction in the presence of iron.

405 Ar derivative isotherms corresponding to samples reacted in the presence of iron and O_2 differ
406 from those measured in the absence of O_2. Changes already appear on sample K-1m-Fe-O_2
407 that displays an additional shoulder at about –6 $\ln P/P_0$ compared to sample K-1-m-Fe. For
408 longer reaction times, derivative isotherms are shifted towards higher adsorbed volumes
409 whereas the peak corresponding to basal faces is displaced towards lower energy.
410 Decomposition results reveal that similar domains as those used in the absence of O_2 are
411 needed for fitting the isotherms, with higher adsorbed volumes on each domain.

412 The important textural changes observed can certainly not be assigned only to clay evolution.
413 In line with TEM results, it could be proposed that the presence of iron oxides and hydroxides
414 are responsible for the increase in SSA. Indeed, such species are known to develop important
415 surface areas as for instance, from 18 to 150 m^2/g for goethite (Prélot et al. 2003, Montes-
416 Hernandez et al. 2004, Larsen and Postma. 2001), from 60 to 150 m^2/g for lepidocrocite
417 (Bonneville et al. 2004; Mäkie et al. 2011), from 30 to 70 m^2/g for hematite and around
418 90 m^2/g for maghemite (Jarlbring et al. 2005, Mäkie et al. 2011). To test this assumption,
419 derivative isotherms for K-3m-Fe-O_2 and K-9m-Fe-O_2 were fitted by least square
420 minimisation, as a linear combination of normalized isotherms obtained on the K-1m sample
421 and on a fresh hydrous iron oxide, characterized in Bottero et al. (1993). As shown in Fig. 6b,
422 such a procedure provides reasonable fits of the experimental isotherms. Such fits can then be
423 used to obtain quantitative estimates of the relative contributions in surface areas of clay
424 phases and iron oxyhydroxides. According to such a treatment, the oxyhydroxide
425 contributions to the total SSA represent 36 and 64% for K-3m-Fe-O_2 and K-9m-Fe-O_2,
426 respectively (Table 3). Consequently, clay phases represent 19.6 and 19.5 m^2/g for K-3m-Fe-
427 O_2 and K-9m-Fe-O_2, respectively. These values are close to that obtained in the absence of

iron (19.3 m^2/g), which suggests that the increase in SSA is entirely due to iron oxyhydroxides formation.

3.2.4. Solid phase chemical analyses

Chemical analyses (Table 4) are normalized by considering constant Al content as no Al was ever detected in solution and no amorphous Al were detected by TEM-EDXS. Only marginal changes are observed in comparison with initial kaolinite. Still they concur with previously presented CEC measurements and solution analyses. Fe is always present in the solid phase whereas contents in both Na and Ca slightly increase in the solid, confirming that both elements likely enter the structure of reacted solid end-products. Investigations were not conducted on samples from oxic reaction.

Particles from K-1m-Fe sample investigated by TEM-EDXS display an average atomic Fe content of 4.5%, with a slight reduction in Al and Si but Al:Si ratio remains constant (Fig. 7). The standard deviation is high, showing a strong heterogeneity in the composition of the neoformed particles. After 3 and 9 months, the average iron content still increases but more moderately and the standard deviation diminishes, revealing some "homogenization" of the particles. In the presence of O_2, system yield similar results than in the absence for one month duration, whereas significant differences are observed for longer times. This is particularly true for Fe content that decreases in the present of O_2 while it increases in its absence after three months of reaction. Furthermore in the former case, the standard deviations are lower, which reveals that more homogeneous products are formed in the presence of O_2. It is very informative to plot the data on a ternary diagram (Fig. 8) that clearly shows that the compositions of reacted clay particles are spread along a mixture line between pure kaolinite and pure berthierine. With O_2 entrance, the composition of the main particles evolves from kaolinite to berthierine in the first month with a reverse evolution for longer times.

3.2.5. XRD and TEM mineralogical analyses

In the absence of iron, no changes are observed on X-ray diffractograms even after 9 months (Fig. 9b). In contrast, the presence of metallic iron leads to significant evolutions. Indeed, the reflection corresponding to the metallic iron peak is strongly reduced in K-1m-Fe and K-1m-Fe-O_2 (Fig. 9c). This reduction continues with increasing reaction times, but is less intense. Whereas metallic iron is still present in the K-9m-Fe sample, iron consumption is faster and complete in K-9m-Fe-O_2. New peaks at 2.97, 2.53 and 2.10 Å corresponding to magnetite appear after one month and slightly increase for longer reaction times. Magnetite and lepidocrocite are already formed in K-1m-Fe-O_2. Then, in K-3m-Fe-O_2, the intensity of the magnetite peak decreases, which is accompanied by a broadening on the wide angle side indicating maghemite formation, thus confirming TEM results. At the same time, peaks corresponding to goethite and hematite appear and their intensities increase in K-9m-Fe-O_2 sample. In the absence of O_2, the 001 peak of kaolinite displays a progressive shift towards higher angles (initial value 7.19 Å, value in K-9m-Fe sample 7.14 Å, Fig 9d). This is associated to the appearance of new peaks (4.69, 3.53, 2.71, 2.53 and 2.15 Å) that grow with increasing time. Such data strongly suggest the formation of a new iron-rich phyllosilicate that, as observed by Perronnet (2004) and Habert (2001), can be identified as either berthierine-1*H* (Brindley and Youell 1953, $(Fe^{2+},Fe^{3+},Al)_3(Si,Al)_2O_5(OH)_4$) a Fe-serpentine or chamosite (Brindley 1949, $(Fe^{2+},Mg,Fe^{3+})_5Al(Si_3Al)O_{10}(OH,O)_8$) a Fe-chlorite. In the presence of O_2, a slight shift towards wider angles of the peak around 7 Å is also observed in K-1m-Fe-O_2. Such an evolution is reversed at longer times as in K-3m-Fe-O_2, the 7 Å peak returns to its initial position. The significant decrease of the 7 Å peak intensity could be due to a loss of crystallinity of the kaolinite in comparison to the initial one or to a lower amount of kaolinite. Nevertheless, the intensity of this peak could also be influenced by orientation effects of the kaolinite platelets in the sample holder during the pattern recording.

On the basis of XRD results only, it is not possible to determine unambiguously whether the neo-formed phyllosilicate is a chlorite or a serpentine. Indeed, in some cases, the 14 Å reflection of chlorite may not diffract due to interference effects. Such a problem can be solved either by using neutron diffraction (Brindley 1982), or by carrying out High Resolution TEM (HRTEM) experiments to directly measure interlayer spacings. This analysis was carried out on more than 40 particles of K-9m-Fe resin embedded sample (Fig. 10). No particles with an interlayer spacing of 14 Å was ever observed and only 7 Å interlayer distances are measured with a mean value of 7.35 ± 0.1 Å. The fact that this value is slightly higher than that obtained by XRD may be assigned to small imperfections in clay orientation perpendicularly to cutting. It can then be safely concluded that the newly formed species belong to the serpentine family. This appears logical considering the temperature range of our experiments. Indeed, in natural systems, chamosite often results from berthierine transformation under reducing conditions at high temperature (160°C for Iijima and Matsumoto 1982, 90°C for Aagaard et al. 2000). This is also the reason why chamosite was observed in the case of iron-smectite interactions at high temperature (300°C, Guillaume et al. 2003).

The progressive shift of the 001 reflection around 7.15 Å and the presence of two distinct 002 reflections at 3.58 Å and 3.53 Å in the XRD pattern may reflect either kaolinite/Fe-serpentine interlayered or separate phases. At a local scale, i.e. for isolated particles of K-9m-Fe sample, SAED (Fig. 11b) recorded perpendicularly to basal planes systematically display a split of diffraction spots of initial kaolinite (Fig. 11a). Such splitted spots clearly show the presence of an additional phase with unit cell close to that of kaolinite and identical crystalline orientations. The additional spots can be assigned to berthierine. It can then be concluded that particles should be considered as mixed systems with epitaxial relationships between kaolinite and Fe-serpentine along basal planes of clay layers.

3.2.6. Spectroscopic analyses

3.2.6.1.Fourier Transformed Infrared Spectroscopy

In the absence of iron no changes are observed on mid-infrared spectra of the samples reacted in comparison with initial kaolinite (Fig. 12). In the presence of iron and under anoxic atmosphere, clear spectra changes can be observed around 3500 cm^{-1} where a broad signal appears and in the Si-O-Si stretching region. In this latter range, two new bands at 1032 and 1008 cm^{-1} appear for K-1m-Fe and K-3m-Fe samples and merge at 1020 cm^{-1} for the K-9m-Fe sample, while a signal at 970 cm^{-1} grows with increasing time. Such changes are markedly different from those observed upon Fe^{3+} enrichment of clay particles (Petit and Decarreau 1990; Petit et al. 1999). They rather correspond to the appearance of a new berthierine-like phase (bands between 3550 and 3400 cm^{-1}, bands at 992 or 950 cm^{-1}, reference spectra in Fig. 12). In the presence of O_2, FTIR spectra of the end-products confirm the previously deduced tendencies. Indeed, the IR spectrum of K-1m-Fe-O_2, is close to that of K-1m-Fe. For K-3m-Fe-O_2 and K-9m-Fe-O_2, the signal at 970 cm^{-1} reduces and changes in the Si-O-Si stretching region are reverse. This then tends to show a consumption of the newly-formed berthierine-like phase even if the hump between 3400 and 3600 cm^{-1} is still visible. This latter signal is then likely due to hydration water.

3.2.6.2.Mössbauer analysis

The spectrum of the initial kaolinite (not shown), despite its very low iron content (0.3%), can be interpreted as corresponding to Fe^{3+}, located in two sites. The first one, with conventional hyperfine parameters (Table 5), can be attributed to octahedral position of the iron in the layer. The second signal presents unusual hyperfine parameters, with a low center shift (0.05 mm/s). It could correspond to Fe localised in tetrahedral layers (Coey, 1980) but it assignment remains ambiguous as previous studies show only octahedral sites in kaolinite (Delineau 1994; Fysh et al. 1983; Cuttler 1980; Janot et al. 1973; Malden and Meads 1967).

The Mössbauer spectrum of K-1m-Fe sample (Fig. 13) is fitted with a sextet corresponding to metallic iron (17% of total Fe) and in three doublets corresponding to Fe in octahedral clay

529 layers under both ferric state (two sites for a total of 36%) and ferrous state (47%). The
530 presence of two Fe^{3+} doublets indicates two distinct environments for Fe in clays (possibly in
531 two different phases). According to literature data (Mackenzie and Berezowski 1983; Kodama
532 et al. 1982; Smyth et al. 1997), the hyperfine parameters of these two latter sites are close to
533 those measured for berthierine or chamosite. The spectra obtained for K-3m-Fe and K-9m-Fe
534 show decreasing iron consumption, as previously observed by XRD. The Fe^{2+}:Fe^{3+} ratio in
535 clays increases between 1 and 3 months and then slightly decreases after 9 months. For the
536 two last samples, small amounts of magnetite are also detected (3% of total iron). Still, as
537 metallic iron is also present, the quantitative determination of magnetite in these latter cases
538 remains approximate (magnetite and metallic iron appear both under a sextet). In the
539 Mössbauer spectrum of sample K-1-m-Fe-O_2, 11% iron is present as metallic iron, 21% as
540 magnetite and 68% in clay particles in octahedral position, with a Fe^{2+}:Fe^{3+} ratio of 0.94.
541 After 3 months of reaction, the proportion of these species evolve with a decrease in both
542 metallic iron and iron in clay minerals (in agreement with TEM results) and an increase of up
543 to 36% of iron in magnetite (non stochiometric magnetite, Zegeye et al. 2011). In terms of
544 hyperfine parameters, the Fe^{2+} signal and one of the Fe^{3+} ones are close to those of berthierine
545 and chamosite after 1 month whereas after 3 months, Fe^{3+} occupies one single site with mean
546 hyperfine parameters values between the two previous set of parameters.

547 *3.2.6.3. XPS*

548 The global XPS spectra are classical (not shown) and reveal the presence of Na, O, Fe, Ti, C
549 (contamination), Si, Al, and traces of Cl and Ca. O appears mainly as OH groups as the fitting
550 of the O 1s peak shows that more than 80% of O is under the form of OH groups. This
551 quantity remains constant with increasing times and similar results are obtained after 1, 3 and
552 9 months. As far as Fe is concerned, the Fe 2p signal is rather complex and is typical of a
553 mixture of both Fe^{2+} and Fe^{3+} with ferrous iron being dominant. There again, it does not
554 evolve significantly with time as the features of Fe 2p band are not significantly modified

555 with increasing reaction time. Average atomic concentrations in Si, Al and Fe are deduced
556 from the XPS spectra, with two data points for each sample (Table 6). In K-1m-Fe sample
557 significant amounts of Fe are observed and the total amount of Fe deduced from XPS spectra
558 increases slightly with increasing reaction time. The amount of Fe "seen" by XPS appears
559 rather high compared with particle composition obtained by TEM-EDXS (Fig. 8), which
560 suggests a surface concentration in Fe species. It must be pointed out that upon the whole
561 reaction, the Al:Si ratio remains constant around 1.0, which confirms XRD and TEM results
562 and is also consistent with the formation of berthierine.

563 ## 4. DISCUSSION

564 Metallic iron corrosion in chloride solution at 90°C without oxygen led to an increase of pH,
565 reductive Eh and to the formation of new iron-rich phases. As expected, magnetite is obtained
566 as a corrosion product in the absence of clay. In the presence of kaolinite, the combination of
567 XRD, FTIR and TEM investigations show that a 7 Å iron-rich clay, belonging to the
568 serpentine family, precipitates. The Fe-serpentine formation from kaolinite is a fast reaction
569 as most of the transformations are observed during the first month. This reaction is also very
570 sensitive to environmental conditions such as Eh, O_2 and time.

571 ### 4.1. Stability of iron-kaolinite system at 90°C

572 Under anoxic atmosphere in chloride solution, anodic iron oxidation and cathodic hydrolysis
573 of water lead to the following relations:

574 $$Fe^0 + 2\ H_2O = H_2 + 2\ OH^- + Fe^{2+}$$

575 $$Fe^0 + 3/2\ H_2O = H_2 + 3\ OH^- + Fe^{3+} \qquad (1)$$

576 Both reactions produce OH^- and H_2, which leads to alkaline and reducing conditions. Eh and
577 pH strongly evolve during the first month and the system stabilizes thereafter with slower
578 evolution. As shown by chemical analyses the iron cations produced are not stable in solution
579 and precipitate as solid corrosion phases. In the absence of clay, iron corrosion is partial,

580 magnetite is the only corrosion product and its precipitation around metallic grains inhibits
581 further oxidation as usually observed (de Combarieu et al. 2007).
582 In the presence of kaolinite and metallic iron at 90°C, magnetite and new iron-rich phases are
583 formed. Kaolinite destabilization is expected as, for similar temperatures, kaolinite dissolution
584 was observed above pH=9 in the absence of iron with dissolution rates that increase with pH
585 (Carroll-Webb and Walther 1988, Carroll and Walther 1990; Huertas et al. 1999). In the
586 presence of iron, OH^- resulting from metallic iron corrosion then may participate to kaolinite
587 destabilization. Actually, kaolinite dissolution rates were measured mostly from dissolved Si
588 and Al (Carroll-Webb and Walther 1988, Carroll and Walther 1990, Bauer and Berger 1998,
589 Huertas et al. 1999). In the case presented here, Si and Al amounts in solution are always very
590 low or null, which shows that both elements resulting from kaolinite dissolution are included
591 in corrosion end-products. In the presence of kaolinite, metallic iron is consumed faster than
592 in the case of iron alone. As microscopic observations reveal rare magnetite agglomerates
593 around pristine iron grains, it can be proposed that this dissolution enhancement is related to
594 the fact that iron grains are not protected by a thick magnetite layer when kaolinite is present.
595 Furthermore, both the consumption of OH^- for kaolinite dissolution and of soluble Fe to form
596 iron rich clays shift reactions (1) towards iron corrosion. It must also be pointed out that the
597 initial destabilization of kaolinite is rather fast as most of the crystallo-chemical modifications
598 are observed during the first month. Such a fast initial step may be due to the close vicinity
599 between iron grains and kaolinite particles in the experimental reactor. Still, the reaction rate
600 strongly decreases after one month, which suggests that the precipitation of iron rich end-
601 products inhibit further iron corrosion and/or kaolinite dissolution.

602 **4.2. From kaolinite to unstable berthierine**

603 The precise nature of the Fe-serpentine depends on its crystal-chemistry, mainly on the
604 distribution of Fe^{2+}, Fe^{3+} and Al^{3+}. In the present case, Al released by kaolinite dissolution is
605 not observed in solution, at the surface of the solid (CEC) or in Al-rich solid phases. Al

Always consult and cite the final, published document. See http://www.minsocam.org or GeoscienceWorld

606 should then be located in the Fe-serpentine phase, which is close to the berthierine end-
607 member. Consequently, the Fe-serpentine will further be referred as to berthierine.
608 The formation of berthierine is not surprising, as this phase was already observed in the
609 context of iron corrosion in the presence of clay at 80°C (Habert 2000; Kohler 2001;
610 Guillaume et al. 2003, 2004; Perronnet 2004; Perronnet et al. 2007; Mösser-Ruck et al. 2010,
611 Osacky et al. 2010), in agreement with the natural formation conditions of berthierine (Iijima
612 and Matsumoto 1982; Hornibrook and Longstaffe 1996; Fritz and Toth 1997; Toth and Fritz
613 1997). In the present study, the obtained berthierines belong to the Fe-berthierine-pole, which
614 is logical, as the system does not contain any significant amount of Mg. Still, as Mg
615 impurities present at the surface of the initial kaolinite are not detected in the liquid phases
616 nor at the surfaces of the solid, small amounts of Mg could be present in octahedral sheets
617 (but they are not detectable by EDXS analyses). An initial system containing more
618 magnesium would likely lead to the formation of Fe-Mg-serpentine, like odinite.
619 In view of the high standard deviations obtained on the TEM-EDX analysis, the clay end-
620 products appear as rather chemically heterogeneous. Furthermore, as shown by the ternary
621 diagrams of Fig. 8, local analyses are spread on a line between kaolinite and berthierine end-
622 members. This strongly suggests that the analysed particles are actually mixtures of kaolinite
623 and berthierine as confirmed by SAED, but with variable relative amounts.
624 More detailed information on the organization of the berthierine layers and their interrelation
625 with kaolinite layers can be obtained from XRD, by modelling the 001 and 002 reflections on
626 the basis of the formalism developed by Drits and Tchoubar (1990) for diffraction by
627 interstratified structures. The random, ordered and demixed modes of stacking were tested by
628 considering a particle made of 45 layers, with a proportion of 80% of kaolinite and 20% of
629 berthierine. Kaolinite structural information was obtained from Bish and Von Dreele (1989).
630 Concerning berthierine, the atomic positions were obtained from the structure of cronstedtite
631 (Hybler 2006), but with a chemical composition derived from the experimental point in the

ternary diagram (Fig. 8) in that is the closest to the berthierine pole. The shift of the 001 reflection towards larger angles and its concomitant widening are well reproduced by the three models (Fig. 14a), which does not allow any clear conclusion on their respective validity. Additional information is derived from a close examination of the 002 region where the existence of two reflections can only be obtained by assuming the existence of a demixed structure. The random and ordered hypothesis being rejected, the segregation hypothesis is further validated by quantitative comparison of 001 and 002 calculated reflections with experimental ones of sample K-1m-Fe. Calculations are carried out by considering particles with mean number of layers of 45 and 30 for kaolinite and berthierine, respectively (see § 4.3 in discussion section). The segregation model can be considered as validated as an acceptable fit (Fig. 14b) is obtained by assuming a mixture with 89% kaolinite and 11% berthierine. It must be pointed out that such relative amounts remain indicative only, as calculated diffraction patterns are extremely sensitive to the chemical composition chosen for the berthierine end member, whose exact crystallographical structure is in addition not available.

A system of kaolinite-berthierine mixed particles with segregated domains is then consistent with all the experimental results. Still, local variations in berthierine composition could also explain the observed heterogeneity. Microspectroscopic analyses would allow testing this assumption.

The newly formed species appear unstable as revealed by its time evolution in terms of both composition (TEM-EDXS) and Fe^{2+}:Fe^{3+} ratio (Mössbauer spectroscopy) with oxygen present. This latter parameter is directly correlated with the solution Eh as shown in Fig. 15. The redox control of kaolinite-berthierine equilibrium is also confirmed by experiments carried out with a slow entrance of O_2 into the reactors that reveal that in such conditions, berthierine is rather unstable. Indeed, in these conditions the first month leads to similar reactions as in the absence of O_2, with a higher consumption of metallic iron. Such higher metallic consumption is also clear for experiments carried out in the absence of clay where

metallic iron is fully consumed to form Fe-oxides and oxyhydroxides. Indeed, in that case, in addition to the anoxic step described by equation 1, another reaction must be considered:

$$3\ Fe^0 + 2O_2 \rightarrow Fe_3O_4 \qquad (2)$$

This latter reaction does not involve any production of either OH^- or H_2, and the pH and Eh can then evolve back towards acidic and oxidizing conditions as observed in the experiments (Fig. 1). These physical-chemical changes lead to the oxidation of magnetite in maghemite and to the decrease in berthierine concentration, which becomes unstable. Iron cations that are released by berthierine destabilization are immediately re-involved in Fe-oxides and hydroxides. Released Si and Al precipitate into kaolinite. Such an evolution continues for longer times and after nine months, berthierine has almost completely disappeared and only few berthierine layers remain (K-9m-Fe-O_2 contained about 1.2% of iron whereas initial kaolinite 0.3%). If longer experiments were carried out, the system would likely evolve to pure kaolinite mixed with iron oxides and hydroxides.

4.3. Structure of Fe-phyllosilicate and relation with initial kaolinite

As discussed in the previous sections, kaolinite-berthierine mixed particles are obtained as a result of iron consumption and kaolinite destabilisation in reductive conditions. Argon adsorption analyses (Table 3) indicate an increase in particles thickness and a decrease in particles length in the presence of iron. The decrease in length is compatible with moderate kaolinite dissolution on edge faces and also shows that berthierine does not form through epitaxial growth on edge faces. In contrast, the concomitant increase in thickness suggests that berthierine grows on basal faces of kaolinite. To check for the consistency of this assumption, and to try to gain further insight into the structure of the formed particles, the numbers of coherent scattering layers in kaolinite and berthierine were calculated from the application of Scherrer's formula to the 002 diffraction peaks in the initial state and after reaction with iron (Table 7). For this, both the anatase contribution to the patterns and baseline were first subtracted. The peak was then decomposed and each component was fitted

684 by a Voigt function whose full width at half maximum (FWHM) is directly used in Scherrer's
685 equation. The number of kaolinite coherent layers appears to slightly decrease with time while
686 the number of coherent berthierine layers remains stable, around 33 layers. The slight
687 decrease in thickness of kaolinite could indicate a moderate dissolution of the initial particles
688 from basal faces in addition to edge dissolution evidenced by argon adsorption. If one
689 assumes that the final particles are formed by adding one mean berthierine (33 layers) and one
690 mean kaolinite (43 layers), the final thickness (corresponding to 76 layers) obtained is close
691 but systematically lower than that derived from argon results (about 90 layers). On the other
692 hand, assuming that a kaolinite particle is sandwiched by two berthierine particles leads to
693 higher thickness. Still, the values obtained are compatible with a mechanism in which
694 berthierine layers crystallize on the basal faces of the initial kaolinite particles. This
695 mechanism is furthermore consistent with the absence of pure end-members revealed by
696 EDXS analyses and SAED patterns as the beams will always go through both berthierine and
697 kaolinite layers, and XRD modeling. In that context, local heterogeneity in Fe-content is due
698 to the various proportions in kaolinite and berthierine thickness in each particle. Such an
699 assumption is also confirmed by XPS analyses which can be considered as a global method
700 enhancing surface chemistry. Indeed, if one plots the XPS-deduced composition on the
701 ternary diagram (Fig. 8), it appears that the measured points fall systematically towards the
702 most iron-rich points. As XPS is a surface technique that probes only the first atomic layers at
703 the surface of the particles after reaction, this shows that Fe, present mainly in a berthierine-
704 like structure, is concentrated at the surface of the particles, which is consistent with
705 berthierine particles developing on the basal faces of kaolinite. Calculations based on XPS
706 analyses show that the atomic ratios obtained can be interpreted as corresponding to kaolinite-
707 berthierine mixtures with an average composition of 70% berthierine and 30% kaolinite. This
708 would rather suggest a scheme in which berthierine grows mainly on one face of kaolinite.
709 However, considering the large beam size used in XPS, the possible contribution of edge

710 faces cannot be completely discarded. The various steps leading to the formation of mixed
711 kaolinite-berthierine particles are schematically represented in Fig. 16.

712 Dissolution of initial kaolinite particles releases Si and Al ions that combine with Fe to
713 form berthierine. According to previous studies in the experimental conditions of the present
714 work, kaolinite dissolution should occur in two steps: (i) a short term dissolution period,
715 during which Si tetrahedra are preferentially dissolved while Al remains poorly soluble and
716 possibly forms Al gel; (ii) a long term congruent dissolution period with a decrease of the
717 reaction rate (Carroll and Walther 1988; Huertas et al. 1999; Bauer and Berger 1998). Still
718 very little indication is provided in these previous studies on the relative contribution of basal
719 and edge surfaces to these two dissolution steps. Morphological and textural data reported in
720 the present work clearly show that kaolinite dissolution is more pronounced on edge than on
721 basal faces as proposed in Fig. 16. This is further confirmed by TEM micrographs of reacted
722 clay particles that exhibit damaged edge faces.

723 As mixed particles are systematically observed, kaolinite particles act as crystallization
724 supports for the iron-rich clay. Our investigations evidence that the precipitation of
725 berthierine occurs on the basal faces of kaolinite. This precipitation mode appears much more
726 favourable for growth than edge faces and may be linked to the differential stability of edge
727 and basal faces of kaolinite as discussed above. It may also be explained by slight difference
728 in unit cell parameters between kaolinite and berthierine (Brindley and Goodyear 1948). The
729 former has a slightly lower basal spacing and a higher extension in the (ab) plane, which
730 limits the growth in continuation of kaolinite layers but is compatible with epitaxial growth on
731 kaolinite basal planes. Nevertheless, precipitation on edges faces cannot be entirely excluded.
732 Mixed particles can be organized with berthierine on either one or both basal faces of
733 kaolinite particles. The apparent initial incongruent dissolution of kaolinite suggests that
734 crystallization of berthierine may be more favourable on Al-OH faces than on Si-O-Si ones.
735 The scheme where berthierine develops on one face only appears then more likely. In that

regard, XPS analysis seems consistent with this assumption but does not provide a definite answer on this aspect. Additional investigations are then necessary to conclude on this particular point.

This study evidenced the high reactivity of the kaolinite-metallic iron system. Nevertheless, one must keep in mind that the experimental ratios (clay:solution and iron:kaolinite were chosen to slightly enhance kinetics and are not representative of the mean conditions expected in waste disposal repository. The influence of such ratios was yet studied by Perronnet (2004) and Pierron (2011). Moreover, in radioactive waste disposal kaolinite will be in mixture with other clay and non-clay minerals which could influence the reactivity of this phase. Whereas the presence of calcite or dolomite does not significantly influence clay-metallic iron interactions (Rivard 2011), introduction of quartz in the system should strongly influence the reaction pathway. Indeed, it was shown that quartz must be absent to form berthierine (Fritz and Toth 1997) and that Fe-serpentines formed during the clay-metallic iron interaction are closer to odinite species in the presence of quartz (Rivard 2011).

5. CONCLUSION

Powdered metallic iron - kaolinite interaction at 90°C in chloride solution and under anoxic atmosphere provokes fast reactions leading to partial metallic iron oxidation and pH increase, magnetite formation in low amount, kaolinite partial dissolution and berthierine formation. Berthierine forms by using Si and Al originating from the alkaline dissolution of kaolinite, mostly from edge surfaces, and Fe released after oxidation of metallic iron by water. Berthierine growths on the basal surfaces of kaolinite particles in epitaxial mode to yield to mixed particles where berthierine layers are located either on one or on both basal faces of kaolinite. The resulting particles exhibit a variable mean composition depending on the relative thickness of berthierine and kaolinite.

The nature of the interaction products remains very sensitive to the oxidation state of the system. Under anoxic atmosphere, berthierine and very low quantities of magnetite are

762 formed. Under oxidising conditions, iron oxides and oxyhydroxides (maghemite, hematite,
763 goethite, lepidocrocite) appear and berthierine becomes unstable leading to the exsolution of
764 iron and the consequent formation of kaolinite.

765 **Acknowledgments**

766 This research was financially supported by Andra (Agence nationale pour la gestion des
767 déchets radioactifs – French national radioactive waste management agency). The authors
768 thank A. Kohler (SCMEM, Université de Lorraine, Vandoeuvre-lès-Nancy, France) for the
769 SEM analyses and A. Renard (LCPME, Université de Lorraine, Vandoeuvre-lès-Nancy,
770 France) for XPS measurements. The authors also thank Y. Moëlo who provided berthierine
771 sample.

772 **References**

773 Aagaard, P., Jahren, J.S., Harstad, A.O., Nilsen, O., and Ramm, M. (2000) Formation of
774 grain-coating chlorite in sandstones. Laboratory synthesized vs. natural occurrences. Clay
775 Minerals, 35, 261-269.

776 Aja, S. U. and Darby Dyar, M. (2002) The stability of Fe-Mg chlorites in hydrothermal
777 solutions – I. Results of experimental investigations. Applied Geochemistry, 17, 1219-
778 1239.

779 Bauer, A. and Berger, G. (1998) Kaolinite and smectite dissolution rate in high molar KOH
780 solutions at 35°C and 80°C. Applied Geochemistry, 13, 905-916.

781 Bish, D.L. and Von Dreele, R.B. (1989) Rietveld refinement of non-hydrogen atomic
782 positions in kaolinite. Clays and Clay Minerals, 37, 289-296.

783 Bonneville, S., Van Cappellen, P., and Behrends, T. (2004) Microbial reduction of iron (III)
784 oxyhydroxides: effects of mineral solubility and availability. Chemical Geology, 212, 255–
785 268.

786 Borden, D. and Giese, R.F. (2001) Baseline studies of the Clay Mineral Society Source Clays:
787 Cation Exchange Capacity measurement by the ammonia-electrode method. Clays and
788 Clay Minerals, 49, 444-445.
789 Bottero, J.Y., Arnaud, M., Villiéras, F., Michot, L.J., de Donato, P., and François, M. (1993)
790 Surface and textural heterogeneity of fresh hydrous ferric oxides in water and in the dry
791 state. Journal of Colloid and Interface Science, 159, 45-52.
792 Brégoin, S. (2003) Variabilité spatiale et temporelle des caractéristiques du Callovo-
793 Oxfordien de Meuse/Haute-Marne. Ph. D. Thesis, ENSMP.
794 Brindley, G.W. (1949) Mineralogy and crystal structure of chamosite. Nature, 164 319-320.
795 Brindley, G.W (1982) Chemical compositions of berthierines-a review. Clays and Clay
796 Minerals, 30, 153-155.
797 Brindley, G. W. and Goodyear, J. (1948) X-ray studies of halloysite and meta-halloysite-II.
798 The transition of halloysite to meta-halloysite in relation to relative humidity.
799 Mineralogical Magazine, 28, 407-422.
800 Brindley, G.W. and R.F. Youell (1953) Ferrous chamosite and ferric chamosite.
801 Mineralogical Magagazine, 37, 57-70.
802 Brunauer, S., Emmett, P.H., and Teller, E. (1938) Adsorption of gases in multimolecular
803 layers. Journal of the American Chemical Society, 60, 309-319.
804 Carroll-Webb, S.A. and Walther, J.V. (1988) A surface complex reaction model for the pH-
805 dependence of corundum and kaolinite dissolution rates. Geochimica et Cosmochimica
806 Acta, 52, 2609-2623.
807 Carroll, S.A. and Walther, J.V. (1990). Kaolinite dissolution at 25°, 60° and 80°C. American
808 Journal of Science, 290, 797-810.
809 Chipera, S.J. and Bish, D.L. (2001) Baseline studies of the Clay Mineral Society Source
810 Clays: Powder X-Ray diffraction analyses. Clays and Clay Minerals, 49, 398-409.

Claret, F., Sakharov, B.A., Drits, B., Meunier, A., Griffault, L., and Lanson B. (2004). Clay minerals in the Meuse-Haute Marne underground laboratory (France): Possible influence of organic matter on clay mineral evolution. Clays and Clay Minerals, 52, 515-532.

Coey, J.M.D. (1980) Clay minerals and their transformations studied with nuclear techniques: The contribution of Mössbauer spectroscopy. Atomic Energy Review, 18, 73-123.

de Combarieu, G, Barboux, P., and Minet, Y. (2007) Iron corrosion in Callovo-Oxfordian argillite: From experiments to thermodynamic/kinetic modeling. Physics and Chemistry of the Earth, 32, 346–358.

Cuttler, A.H. (1980) The behaviour of a synthetic ^{57}Fe doped kaolin: Mössbauer and electron paramagnetic resonance studies. Clay Minerals, 15, 429-444.

Delineau, T. (1994) Les argiles kaoliniques du Bassin des Charentes (France) : Analyses typologique, cristallochimique, spéciation du fer et applications. Ph.D. Thesis INPL.

Drits, V.A. and Tchoubar, C. (1990) Determination of the Structural Characteristics of Mixed-Layer Minerals. In X-Ray Diffraction by Disordered Lamellar Structures. Springer Verlag, p. 305-360.

Farmer, V.C. (1974) Layer silicates. In infrared Spectra of Minerals (EDX Farmer V.C.) Mineralogical Society, London, p. 331-363.

Fritz, S.J. and Toth, T.A. (1997) An Fe-bertherine from Cretaceous laterite: Part II. Estimation of Eh, pH and pCO_2 conditions of formation. Clays and Clay Minerals, 45, 580-586.

Fysh, S.A., Cashion, J.D., and Clark, P.E. (1983) Mössbauer effect studies of iron in kaolin. I. Structural iron. Clays and Clay Minerals, 31, 4, 285-292.

Gaucher, E., Robelin, C., Matray, J.M., Négrel, G., Gros, Y., Heitz, J.F., Vinsot, A., Rebours, H., Cassagnabère, A., and Bouchet, A. (2004) ANDRA underground research laboratory: interpretation of the mineralogical and geochemical data acquired in the Callovian–

836 Oxfordian formation by investigative drilling. Physics and Chemistry of the Earth, 29, 55-
837 77.
838 Guillaume, D. (2002) Etude expérimentale du système fer – smectite en présence de solution
839 à 80 °C et 300 °C. Ph.D. Thesis. Univ. Henri Poincaré Nancy I.
840 Guillaume, D., Neaman, A., Cathelineau, M., Mösser-Ruck, R., Peiffert, C., Abdelmoula, M.,
841 Dubessy, J., Villiéras, F., Baronnet, A., and Michau, N. (2003) Experimental synthesis of
842 chlorite from smectite at 300°C in the presence of metallic Fe. Clay Minerals, 38, 281-302.
843 Guillaume, D., Neaman, A., Cathelineau, M., Mösser-Ruck, R., Peiffert, C., Abdelmoula, M.,
844 Dubessy, J., Villiéras, F., and Michau, N. (2004). Experimental study of the transformation
845 of smectite at 80°C and 300°C in the presence of Fe oxides. Clay Minerals, 39, 17-34.
846 Habert, B. (2000) Réactivité du fer dans les gels et les smectites. Ph. D. Thesis Univ Paris 6.
847 Hassan, M.S., Villieras, F., Razafitianamaharavo, A., and Michot, L.J. (2005) Role of
848 exchangeable cations on geometrical and energetic surface heterogeneity of kaolinites.
849 Langmuir, 21, 26, 12283-12289.
850 Hybler J. (2006) Parallel intergrowths in cronstedtite-1T: determination of the degree of
851 disorder. European Journal of Mineralogy, 18, 197-205.
852 Hornibrook, E.R.C., and Longstaffe, F.J. (1996) Berthierine from the lower cretaceous
853 Clearwater formation, Alberta, Canada. Clays and Clay Minerals, 44, 1, 1-21.
854 Huertas, F.J., Chou, L., and Wollast, R. (1999) Mechanism of kaolinite dissolution at room
855 temperature and pressure Part II: Kinetic study. Geochimica et Cosmochimica Acta, 63,
856 19/20, 3261-3275.
857 Iijima, A. and Matsumoto, R. (1982). Berthierine and chamosite in coal mesures of Japan.
858 Clays and Clay Minerals, 30, 4, 264-274.
859 Janot, C., Gilbert, H., and Tobias, C. (1973) Caractérisation de kaolinites ferrifères par
860 spectrométrie Mössbauer. Bulletin de la Societe Francaise de Mineralogie et de
861 Cristallographie, 96, 281-291.

Jarlbring, M., Gunneriusson, L., Hussmann, B., and Forsling, W. (2005) Surface complex characteristics of synthetic maghemite and hematite in aqueous suspensions. Journal of Colloid and Interface Science, 285, 212–217.

Kodama, H., Longworth, G., and Townsend, M.G. (1982) A Mossbauer investigation of some chlorites and their oxidation products. Canadian Mineralogist, 20, 4, 585-592.

Kohler, E. (2001) Réactivité des mélanges synthétiques smectite/kaolinite et smectite/aluminium gel en présence d'un excès de fer métal. DRRT génie des matériaux. Univ Evry Val d'Essonne.

Landais, P. (2006) Advances in geochemical research for the underground disposal of high-level, long-lived radioactive waste in clay formation. Journal of Geochemical Exploration, 88, 32- 36.

Lantenois, S., Lanson, B., Muller, F., Bauer, A., Jullien, M., and Plançon, A. (2005) Experimental study of smectite interaction with metal Fe at low temperature: 1. Smectite destabilization. Clays and Clay Minerals, 53, 6, 597-612.

Larsen, O. and Postma, D. (2001) Kinetics of reductive bulk dissolution of lepidocrocite, ferrihydrite, and goethite. Geochimica et Cosmochimica Acta, 65, 9, 1379-2001.

Mackenzie, K.J.D. and Berezowski, R.M. (1983) Thermal and Mossbauer studies of iron-containing hydrous silicates. V. Berthiérine. Thermochimica Acta, 74, 291-312.

Mäkie, P., Wesin, G., Persson, P., and Osterlund, L. (2011) Adsorption of Trimethyl Phosphate on Maghemite, Hematite, and Goethite Nanoparticles. Journal of Physical Chemistry, A 115, 8948-8959.

Malden, P.J. and Meads, R.E. (1967) Substitution by iron in kaolinite. Nature, 215, 844-846.

Mantin, I. (1969) Mesure de la capacité d'échange des minéraux argileux par l'éthylène diamine et les ions complexes de l'éthylène diamine. Comptes Rendus des Séances de l'Académie des Sciences, Série D: Sciences Naturelles, 269, 815-818.

887 Mantin, I. and Glaeser, R. (1960) Fixation des ions cobaltihexamines par les montmorillonites
888 acides. Bulletin du Groupe Francais des Argiles, 12, 188.
889 Mermut, A.R. and Cano, A.F. (2001) Baseline studies of the Clay Mineral Society Source
890 Clays: Chemical analyses of major elements. Clays and Clay Minerals, 49, 5, 381-386.
891 Michot, L.J., François, M., and Cases, J.M. (1990) Continuous volumetric procedure for gas
892 adsorption. A mean to study surface heterogeneity. Langmuir, 6, 677-681.
893 Montes-Hernandez, G., Beeck, P., Renard, F., Quirico, E., Lanson, B., Chiriac, R., and
894 Findling, N. (2004) Fast Precipitation of Acicular Goethite from Ferric Hydroxide
895 Gelunder Moderate Temperature (30 and 70 °C). Crystal Growth & Design, 11, 2264–
896 2272.
897 Morel, L.R. (1957) Etude expérimentale des phénomènes d'échange sur différents minéraux
898 argileux. Annales Agricoles, 8, 5-90.
899 Mosser-Ruck, R., Cathelineau, M, Guillaume, D., Charpentier, D., Rousset, D., Barres, O.,
900 and Michau, N. (2010) Effects of temperature, pH, and iron-clay and liquid-clay ratios on
901 experimental conversion of dioctahedral smectite to berthierine, chlorite, vermiculite, or
902 saponite. Clays and Clay Minerals, 58, 280-291.
903 Osacky, M., Sucha, V., Czimerova, A., and Madejova, J. (2010) Reaction of smectites with
904 iron in a nitrogen atmosphere at 75°C. Applied Clay Science, 50, 237-244.
905 Perronnet, M. (2004) Réactivité des matériaux argileux dans un contexte de corrosion métal.
906 Application au stockage des déchets radioactifs en site argileux, 280 p. Ph.D. Thesis, INPL
907 Nancy, France.
908 Perronnet, M., Villieras, F., Jullien, M., Razafitianamaharavo, A., Raynal, J., and Bonnin, D.
909 (2007) A link between the energetic heterogeneities of the edge faces of smectites.
910 Geochimica et Cosmochimica Acta, 71, 1463-1479.
911 Petit, S. and Decarreau, A. (1990) Hydrothermal (200°C) synthesis and crystal chemistry of
912 iron-rich kaolinites. Clay Minerals, 25, 181-196.

913 Petit, S., Madelova, J., Decarreau, A., and Martin, F. (1999) Characterization of octahedral
914 substitutions in kaolinites using near infrared spectroscopy. Clays and Clay Minerals, 47,
915 130-108.
916 Pierron, O. (2011) Interactions eau-fer-argilite : rôle des paramètres liquide/roche, fer/argilite,
917 température sur la nature des phases minérales, 226 p Ph.D Thesis, Université Nancy I,
918 France.
919 Prélot, B., Villiéras, F., Pelletier, M., Gérard, G., Gaboriaud, F., Ehehardt, J.J., Perrone, J.,
920 Fedoroff, M., Jeanjean, J., Lefèvre, G., Mazerolles, L., Pastol, J.L., Rouchaud, J.C., and
921 Lindecker, C. (2003) Morphology and surface heterogeneities in synthetic goethites.
922 Journal of Colloid and Interface Science, 261, 244-254.
923 Rivard, C. (2011) Contribution à l'étude de la stabilité des minéraux constitutifs de l'argilite
924 du Callovo-Oxfordien en présence de fer à 90°C, 338 p Ph.D Thesis, INPL Nancy, France.
925 Rousset, D. (2002) Etude de la fraction argileuse de séquences sédimentaires de la Meuse et
926 du Gard. Reconstitution de l'histoire diagénétique et des caractéristiques physico-
927 chimiques des cibles. Aspects minéralogiques, géochimiques et isotopiques, 270 p. Ph.D.
928 Thesis, Université Louis Pasteur, Strasbourg, France.
929 Russell, J.D. and Fraser, A.R. (1994) Infrared methods. In Clay Mineralogy: Spectroscopic
930 and Chemical Determinative Methods, EDX. M.J. Wilson, p. 11-67. Chapman & Hall,
931 London.
932 Sammartino, S. (2001) Construction d'un modèle conceptuel de la porosité et de la
933 minéralogie dans les argilites du site de Bure, Rapport Andra n°D.RP.0ERM.01.018.
934 Savage, D., Watson, C., Benbow, S., and Wilson, J. (2010) Modelling iron-bentonite
935 interactions. Applied Clay Science, 47, 91-98.
936 Sayed-Hassan, M. (2005) Etude des hétérogénéités morphologiques et énergétiques
937 superficielles des kaolinites par AFM et adsorption de gaz. Ph.D. Thesis. INPL Nancy,
938 France.

939 Sayed-Hassan, M., Villieras, F., Gaboriaud, F., and Razafitianamaharavo, A. (2006) AFM and
940 low-pressure argon adsorption analysis of geometrical properties of phyllosilicates. Journal
941 of Colloid and Interface Science, 296, 614-623.
942 Schlegel, M. L., Bataillon, C., Benhamida, K., Blanc, C., Menut, D., and Lacour, J.L. (2008)
943 Metal corrosion and argillite transformation at the water-satured, high temperature iron-
944 clay interface: A microscopic-scale study. Applied Geochemistry, 23, 2619-2633.
945 Smyth, J.R., Dyar, M.D., May, H.M., Bricker, O.P., and Acker, J.G. (1997) Crystal structure
946 refinement and Mössbauer spectroscopy of an ordered, triclinic clinochlore. Clays and
947 Clay Minerals, 45, 4, 544-550.
948 Toth, T.A. and Fritz, S.J. (1997) An Fe-bertherine from Cretaceous laterite: Part I.
949 Characterization. Clays and Clay Minerals, 45, 4, 564-579.
950 Van der Marel, H.W. and Beutelspacher, H. (1976) Atlas of infrared spectroscopy of clay
951 minerals and their admixtures, Amsterdam.
952 Villiéras, F., Cases, J.M., François, M., Michot, L.J., and Thomas, F. (1992) Texture and
953 surface energetic Heterogeneity of solids from modelling of low pressure gas adsorption
954 isotherms. Langmuir 8, 1789
955 Villiéras, F., Michot, L.J, Bardot, F., Cases, J.M., François, M., and Rudzinski W. (1997a) An
956 improved derivative isotherm summation method to study surface heterogeneity of clay
957 minerals. Langmuir, 8, 1104-1117.
958 Villiéras, F., Michot, L.J., Cases J.M, Bérend, I., Bardot, F., François, M., and Yvon J.
959 (1997b) Static and dynamic studies of the energetic surface heterogeneity of clay minerals.
960 Studies in Surface Science and Catalysis, 104, 573-623.
961 Villiéras, F., Mamleev, V.S., Nicholson, D., and Cases, J. M. (2002) Adsorption of Spherical
962 Molecules in Probing the Surface Topography: 2. Model of Conditional Probabilities
963 Langmuir 18, 3963-3979.

964 Yven, B., Sammartino, S., Géraud, Y., Homand, H., and Villiéras, F. (2007) Mineralogy,
965 Texture and Porosity of Callovo-Oxfordian Argillites of the Meuse/Haute-Marne Region
966 (Eastern Paris Basin) Mémoires de la Société Géologique de France, 178, 73-90.
967 Zegeye, A., Abdelmoula, M., Usman, M., Hanna, K., and Ruby, C. (2011) In situ monitoring
968 of lepidocrocite bioreduction and magnetite formation by reflection Mössbauer
969 spectroscopy. American Mineralogist, 96, 1410–1413.
970

971 Annex 1.

972 Table 1. Main parameters obtained from the application of the DIS method (BET–Hill
973 model) to Argon adsorption isotherms at 77 K on initial kaolinite and by-products. SSA are
974 given in m^2/g of clays (correction thanks to XRD and Mössbauer data)

Sample	maximum position	lateral interactions	adsorbed volume	local SSA (m^2/g)	total SSA (m^2/g)
	Ln(P/P_0)	w/kT	Wm (cm^3/g)		
1 m	-11,65	-0,20	0,07	0,3	19.3
	-9,80	0,00	0,05	0,2	
	-7,78	0,00	0,22	0,8	
	-5,75	0,70	0,52	1,9	
	-4,37	1,60	1,77	6,5	
	-3,70	1,60	0,93	3,4	
	-2,37	0,00	1,65	6,1	
1 m-Fe	-12,80	0,00	0,06	0,2	17.2
	-9,75	-0,90	0,10	0,4	
	-7,80	-0,30	0,39	1,5	
	-5,74	1,10	0,70	2,6	
	-4,58	1,40	1,26	4,7	
	-3,61	1,40	0,44	1,6	
	-2,41	0,00	1,36	5,0	
3 m-Fe	-12,38	1,00	0,03	0,1	16.0
	-9,82	-1,10	0,15	0,6	
	-7,70	0,20	0,27	1,0	
	-5,64	1,00	0,94	3,5	
	-4,49	1,60	1,03	3,8	
	-3,62	1,60	0,33	1,2	
	-2,41	0,00	1,39	5,2	
9 m-Fe	-12,52	-0,20	0,05	0,2	17.2
	-9,78	-1,10	0,18	0,7	
	-7,44	0,00	0,35	1,3	
	-5,47	0,90	0,88	3,3	
	-4,41	1,60	1,18	4,4	
	-3,61	1,60	0,32	1,2	
	-2,41	0,00	1,50	5,6	
1 m-Fe-O_2	-12,37	-0,20	0,06	0,2	18.4
	-9,28	0,00	0,20	0,8	
	-7,46	0,90	0,27	1,0	
	-5,65	1,10	1,26	4,7	
	-4,44	1,60	1,19	4,4	
	-3,60	1,60	0,28	1,0	
	-2,43	0,00	1,33	4,9	
3 m-Fe-O_2	-13,02	0,9	0,14	0,5	33.8
	-9,79	-0,3	0,48	1,8	
	-7,44	0,3	0,64	2,4	
	-5,75	0,8	0,89	3,3	
	-4,36	1,6	2,55	9,5	
	-3,62	1,6	0,57	2,1	
	-2,42	0,00	2,96	11,0	
9 m-Fe-O_2	-13,50	0,70	0,27	1,0	58.5
	-10,53	-0,70	1,22	4,5	
	-7,46	0,00	1,96	7,3	
	-5,52	0,80	1,60	5,9	
	-4,44	1,60	2,50	9,3	
	-3,64	1,60	1,84	6,8	
	-2,41	0,00	4,63	17,2	

975 Fig. 1. pH and Eh evolution of metallic iron supernatants (a) and kaolinite supernatants after
976 reaction in the presence of iron or not (b), as a function of the presence of O_2 and time.

977 Fig. 2. SEM micrographs of end-products: (a) magnetite agglomerates in K-Fe-9m, (b) coarse
978 fraction of K-1m-Fe, (c) detail on clays aggregate in K-9m-Fe and (e) fraction of K-9m-Fe
979 in resin. (d), is a TEM micrograph of an ultrathin cut of a clay nodule (along the line
980 indicated on Fig. 2) of coarse fraction of K-1m-Fe (d), EDXS analyse of clay particles at the
981 end of the arrow indicates 62.8% of O, 7.5% of Al %, 7.6 of Si and 22.1% of Fe (atomic
982 percentage).

983 Fig. 3. CEC_{Cat} evolution as a function of the presence of iron, O_2 and time in kaolinite and
984 end-products.

985 Fig. 4. Fine fractions TEM micrographs. (a) initial kaolinite, (b) K-1m-Fe, (c) K-9m-Fe, (d)
986 K-3m-Fe-O_2 and (e) K-9m-Fe-O_2; arrows indicate iron oxides and hydroxides.

987 Fig. 5. Adsorption-desorption N_2 isotherms of initial kaolinite and end-products (a) and
988 evolution of SSA calculated by BET method as function of the presence of O_2 and time (b).

989 Fig. 6. (a) Experimental derivatives of low pressure argon adsorption isotherms, (b)
990 experimental derivative argon adsorption isotherms and decomposition by DIS method of K-
991 1m and (c) argon derivative isotherms of K-3 and K-9m-Fe-O_2 (solid lines) and
992 corresponding fittings (dashed line). Isotherms are fitted with linear combination of
993 normalized isotherms obtained on K-1m and on an iron oxyhydroxide (dark and light grey
994 lines respectively).

995 Fig. 7. Al, Si and Fe atomic percentage in clay particles of initial kaolinite and end-products
996 using TEM-EDXS (average on 20 particles) as a function of the presence of O_2 and time.

997 Fig. 8. Al-Si-Fe ternary diagram of 1:1 Fe-silicates references and end-products (TEM-EDXS
998 and XPS analyses), in the absence of O_2 (a) and in the presence (b). End-products are
999 represented by filled symbols: orange triangles up for K-1m-Fe and K-1m-Fe-O_2, red

1000 triangles down for K-3m-Fe and K-3m-Fe-O_2, brown diamonds for K-9m-Fe and K-9m-Fe-
1001 O_2. Literature references are represented by empty symbols: circles for berthierine (Brindley
1002 1982 and Saint-Aubin berthierine (characterized in an oral contribution from Moëlo Y. at
1003 French Clay Group meeting in 2009), triangle up for odinite, diamond for cronstedtite and
1004 square for greenalite.

1005 Fig. 9. (a) Disoriented powder XRD of initial kaolinite and end-products, (b) enlargement of
1006 001 reflection around 7 Å and (c) normalised integrated intensity of principal metallic iron
1007 reflection around 52 Å as function of the presence of O_2 and time.

1008 Fig. 10. HRTEM micrograph of K-9m-Fe clay particles in ultrathin section.

1009 Fig. 11. TEM micrographs (top) and corresponding SAED patterns (bottom) of particles of (a)
1010 initial kaolinite and (b) K-9m-Fe. The content in iron of the K-9m-Fe probed particle is
1011 4.3% (atomic percentage), k and b indicate kaolinite (triclinic system) and berthierine
1012 (hexagonal system) planes, respectively.

1013 Fig. 12. Comparison between diffuse reflectance FTIR spectra of initial kaolinite, end-
1014 products and standards as a function of the presence of O_2 and time. Chamosite Aja (Aja and
1015 Darby Dyar 2002) is pure, berthierine Ryan comprises calcium phosphate, calcite, siderite
1016 and fayalite. Saint-Aubin berthierine comprises less than 5 % of kaolinite.

1017 Fig. 13. Mössbauer spectra of end-products (reaction in the presence of iron) acquired at room
1018 temperature.

1019 Fig. 14. Modeling of the 001 and 002 reflections of clay particles in a berthierine-kaolinite
1020 mixture (after anatase reflection subtracted). (a) calculations for different stacking statistics.
1021 (b) pattern modeling of sample K-1m-Fe assuming a segregated structure.

1022 Fig. 15. Eh end-products supernatants evolution as a function of the Fe^{2+}:Fe^{3+} ratio in clay
1023 particles.

1024 Fig. 16. Proposed mechanism for the transformation of kaolinite into a mixture of berthierine-
1025 kaolinite in the presence of metallic iron under anoxic atmosphere.

1026 Table 2. Chemistry of the initial and experimental solutions after reaction of (i) single metallic iron, (ii) kaolinite without iron and (iii)
1027 kaolinite with iron, function of the presence of O_2 and time. Eh are in mV, conductivities in mS/cm and concentrations in mg/L. In the presence
1028 of O_2, concentrations are recalculated taking account water losses.

	pH	Eh	conductivity	Na	K	Ca	Mg	Al	Fe	Fe^{2+}	Si	Na:Ca
Initial solution (calculated values)	-	-	-	476	-	152	-	-	-	-	-	3.13
Single metallic iron												
Initial solution (measured values)	7.25	-115	2.9	442	1.62	149	< 0.5	< 1	0.68	-	0.07	2.97
Fe-1.2m	8.95	-288	3.0	465	1.69	163	< 0.5	< 1	0.08	0.07	0.15	2.85
Fe-3m	8.76	-386	2.6	474	1.21	159	< 0.5	< 1	0.09	0.10	0.28	2.98
Fe-9m	8.84	-263	2.5	457	1.55	152	< 0.5	< 1	0.03	0.03	0.15	3.01
Fe-1m-O_2	4.99	125	2.8	-	-	-	-	-	-	-	-	-
Fe-4 m-O_2	6.20	55	3.3	-	-	-	-	-	-	-	-	-
Fe-10 m-O_2	6.60	6.80	9.1	1514	21.03	442	0.62	< 1	4.17	4.10	2.15	3.43
Kaolinite												
Initial solution (measured values)	-	-	-	449	11.2[a]	139	< 0.5	< 1	0.04	-	0.04	3.2
Initial equilibrated solution [b]	3.98	184	2.7	462	3.1	132	1.7	1.5	0.43	-	1.7	3.5
K-1m	3.49	174	3.1	412	4.6	113	1.6	< 1	0.28	0.32	0.8	3.7
K-3m	3.70	193	3.0	458	3.7	130	1.6	< 1	0.21	0.26	0.8	3.5
K-9m	3.71	199	3.2	366	3.9	102	1.6	< 1	0.24	0.26	1.7	3.6
K-1m-Fe	9.07	-214	2.4	445	2.3	130	< 0.5	< 1	0.10	0.07	0.7	3.4
K-3m-Fe	8.59	-306	2.3	466	3.6	87[a]	< 0.5	< 1	0.05	0.02	0.6	5.4
K-9m-Fe	7.86	-233	2.9	510	2.1	135	< 0.5	< 1	0.49	0.43	1.0	3.8
K-1m-Fe-O_2	7.55	-22	2.5	421	6.2	105	< 0.5	< 1	0.42	-	0.9	4.0
K-3m-Fe-O_2	6.23	53	2. 9	494	4.8	130	1.3	< 1	24.60[a]	25.60 [a]	2.4	3.8
K-9m-Fe-O_2	4.39	158	3.3	540	4.8	140	2.7	< 1	1.22	1.30	28.0 [a]	3.9
Error	0.05	5	0.1	5%	2%	2%	2%	10%	5%	5%	10%	-

(-) Not analysed.

(a) Doubtful results due to possible remaining colloids in the solution.

(b) After equilibration with kaolinite for 24 hours at ambient temperature.

Table 3. CEC and exchangeable cations of initial kaolinite and end-products, in meq per 100 g of sample.

	$CEC_{A472\text{-}Co}$	CEC_{Cat}	Na	K	Ca	Mg	Al	Fe	Si	Na:Ca
Raw kaolinite	2.8	1.3	0.03	0.04	0.27	0.29	0.69	< 0.02	< 0.3	0.1
Initial equilibrated kaolinite[a]	2.1	4.0	1.39	0.01	1.80	0.04	0.80	< 0.02	-	0.8
K-1m	2.9	3.9	1.82	0.04	2.00	0.05	< 0.2	< 0.02	< 0.3	0.9
K-3m	2.7	4.1	1.85	0.12	2.07	0.05	< 0.2	< 0.02	< 0.3	0.9
K-9m	2.1	3.7	1.63	0.09	1.93	0.05	< 0.2	< 0.02	< 0.3	0.8
Calculated initial equilibrated Kaolinite with iron (75% of clay)[a]	1.6	3.0	1.04	0.01	1.35	0.03	0.6	< 0.02	-	0.8
K-1m-Fe	24.3	2.8	1.64	0.01	1.18	< 0.01	< 0.2	< 0.02	< 0.3	1.4
K-3m-Fe	20.7	2.8	1.69	0.04	1.07	0.01	< 0.2	< 0.02	< 0.3	1.6
K-9m-Fe	19.3	3.0	1.82	0.02	1.19	< 0.01	< 0.2	< 0.02	< 0.3	1.5
K-1m-Fe-O_2	30.8	3.0	1.88	0.03	1.02	0.01	< 0.2	0.04	< 0.3	1.8
K-3m-Fe-O_2	16.8	4.0	2.33	0.05	1.56	0.03	< 0.2	0.01	< 0.3	1.5
K-9m-Fe-O_2	3.7	4.8	2.49	0.07	2.12	0.08	< 0.2	< 0.02	< 0.3	1.2
Error	0.2	0.2	0.002	0.001	0.002	0.0003	0.07	0.003	0.1	

(-) Not analysed.

(a) After equilibration with chloride solution for 24 hours at ambient temperature.

Table 4. SSA and morphological parameters of initial kaolinite and end-products, obtained by nitrogen adsorption and by applying the DIS method (BET–Hill model) to argon adsorption isotherms at 77 K. SSA are given in m^2/g of clays (correction thanks to Mössbauer data), except in the first column which are in m^2/g of sample. In the presence of O_2, the last columns list the SSA contributions obtained by fitting the Ar isotherms as a linear combination of normalized isotherms (Ar DIS SSA LS) of sample K-1m and of an iron oxyhydroxide.

	N_2 BET SSA		Ar DIS SSA	Basal SSA	Edge SSA	lamellarity index (%)	length (nm)	thickness (nm)	mean number of 7 Å layers
	m^2/g of sample	m^2/g of clays							
initial kaolinite	20.5	20.5	-	-	-	-	-	-	-
K-1m	19.3	19.3	19.3	16.1	3.2	83	472	47	65
K-3m	20.5	20.5	-	-	-	-	-	-	-
K-9m	21.1	21.1	-	-	-	-	-	-	-
K-1m-Fe	17.7	19.0	17.2	11.8	5.5	68	320	55	82
K-3m-Fe	17.7	18.4	16.0	10.4	5.6	65	298	65	95
K-9m-Fe	18.2	18.9	17.2	11.3	5.9	66	279	60	86

	N_2 BET SSA		Ar DIS SSA	Ar DIS SSA LS contribution from oxyhydroxides (%)	Ar DIS SSA LS contribution from clay (%)
	m^2/g of sample	m^2/g of clays			
K-1m-Fe-O_2	20.2	29.7	18.4	-	-
K-3m-Fe-O_2	33.6	57.9	33.8	36	64
K-9m-Fe-O_2	53.4	-	58.5	61	39
Error	0.8	0.8	0.8	-	-

(-) Not analysed or not calculated.

1042 Table 5. Chemistry of initial kaolinite and end-products (in molar percentage).

	Na	K	Ca	Mg	Fe	Al	Si	Ti	P	Total
KGa-2 (Mermut and Cano 2001)	0.13	0.03	0.04	0.07	0.95	49.44	47.92	1.13	0.30	100.0
KGa-2 initial	0.02	0.06	0.03	0.05	0.9	48.8	50.2	-	-	100.0
K-1m	0.15	0.06	0.07	0.04	0.9	48.8	50.0	-	-	100.1
K-3m	0.17	0.06	0.09	0.04	0.9	48.8	50.2	-	-	100.3
K-9m	0.15	0.06	0.08	0.04	0.9	48.8	49.6	-	-	99.7
K-1m-Fe	0.28	0.06	0.12	0.05	27.9	48.8	50.9	-	-	128.2
K-3m-Fe	0.44	0.06	0.14	0.05	28.7	48.8	50.9	-	-	129.1
K-9m-Fe	0.28	0.06	0.15	0.05	29.0	48.8	50.8	-	-	129.2
Error	10%	10%	10%	5%	1%	0.5%	0.5%	-	-	-

1043 (-) Not analysed.

1044 Table 6. Mössbauer hyperfin parameters, corresponding attributions and relative abundance of components in initial kaolinite and end-products.

1045 CS: Center shift, QS: quadrupole splitting and H: hyperfine magnetite field.

	CS (mm/s)	QS (mm/s)	H (kOe)	Attribution	Relative abundance (%)	Fe^{2+} : Fe^{3+} ratio in clays	Proportion of the non-clay minerals in the sample (%)
initial	0.30	0.31	-	Fe^{3+} VI	67.2 ± 3.5		
	0.05	0.50	-	Fe^{3+} IV	32.8 ± 3.9		
K-1m-Fe	1.13	2.49	-	Fe^{2+} VI	47.0 ± 1.0	1.3	
	0.26	0.27	-	Fe^{3+} VI	24.2 ± 1.5		
	0.33	0.88	-	Fe^{3+} VI	12.3 ± 1.4		
	0	0	330	metallic iron	16.5 ± 1.4		4.4
K-3m-Fe	1.11	2.53	-	Fe^{2+} VI	66.6 ± 1	3.5	
	0.25	0.29	-	Fe^{3+} VI	12.2 ± 1.5		
	0.38	0.82	-	Fe^{3+} VI	7.0 ± 1.0		
	0	0	331	metallic iron	11.2 ± 3.1		2.8
	0.5	0.003	472	magnetite	3 ± 1		2.7
	0.5	0.05	452				
K-9m-Fe	1.13	2.53	-	Fe^{2+} VI	61.1 ± 2.5	2.0	
	0.25	0.29	-	Fe^{3+} VI	22.1 ± 2		
	0.38	0.99	-	Fe^{3+} VI	7.3 ± 1		
	0	0	331	metallic iron	6.5 ± 1.5		1.8
	1.3	0	490	magnetite	3 ± 1		2.7
	0.5	0	450				
K-1m-Fe-O_2	1.12	2.51	-	Fe^{2+} VI	33.4 ± 1.8	0.94	
	0.46	0.72	-	Fe^{3+} VI	16.1 ± 2		
	0.22	0.43	-	Fe^{3+} VI	19.0 ± 1		

	0	0	332	metallic iron	10.8 ± 2.3		3
	0.30	0	491	magnetite	6.6 ± 4		5
	0.58	0	452		14.1 ± 7		
	1.12	2.43	-	Fe^{2+} VI	20.1 ± 1.7		
	0.33	0.65	-	Fe^{3+} VI	38.7 ± 1.3	0.51	
K-3m-Fe-O_2	0	0	324	metallic iron	7.7 ± 1.6		2
	0.32	0	484	non stochiometric magnetite[a]	13.0 ± 2.1 20.5 ± 2.3		9

(-) Inapplicable

(a) See Zegeye et al. 2011.

Table 7. Atomic contents and ratios deduced from the analysis of XPS spectra.

	initial	K-1m-Fe	K-3m-Fe	K-9m-Fe
Si	13.4	8.6	7.7	8.1
Al	13.6	8.7	8.3	8.5
Fe	-	6.2	6.5	7.0
Al/Si	1.0	1.0	1.1	1.1
Si/Fe	-	1.4	1.2	1.2
Al/Fe	-	1.4	1.3	1.2

(-) Not detected.

1051 Table 8. Number of coherent layers deduced from calculation of Scherrer index on fitted

1052 002 diffraction peaks and mean number of 7 Å layers deduced from Ar adsorption analyses.

	Number of coherent layers		Ar mean number of 7 Å layers
	kaolinite	berthierine	
Initial kaolinite	48	-	65
K-1m-Fe	44	33	82
K-3m-Fe	43	35	95
K-9m-Fe	42	31	86

1053

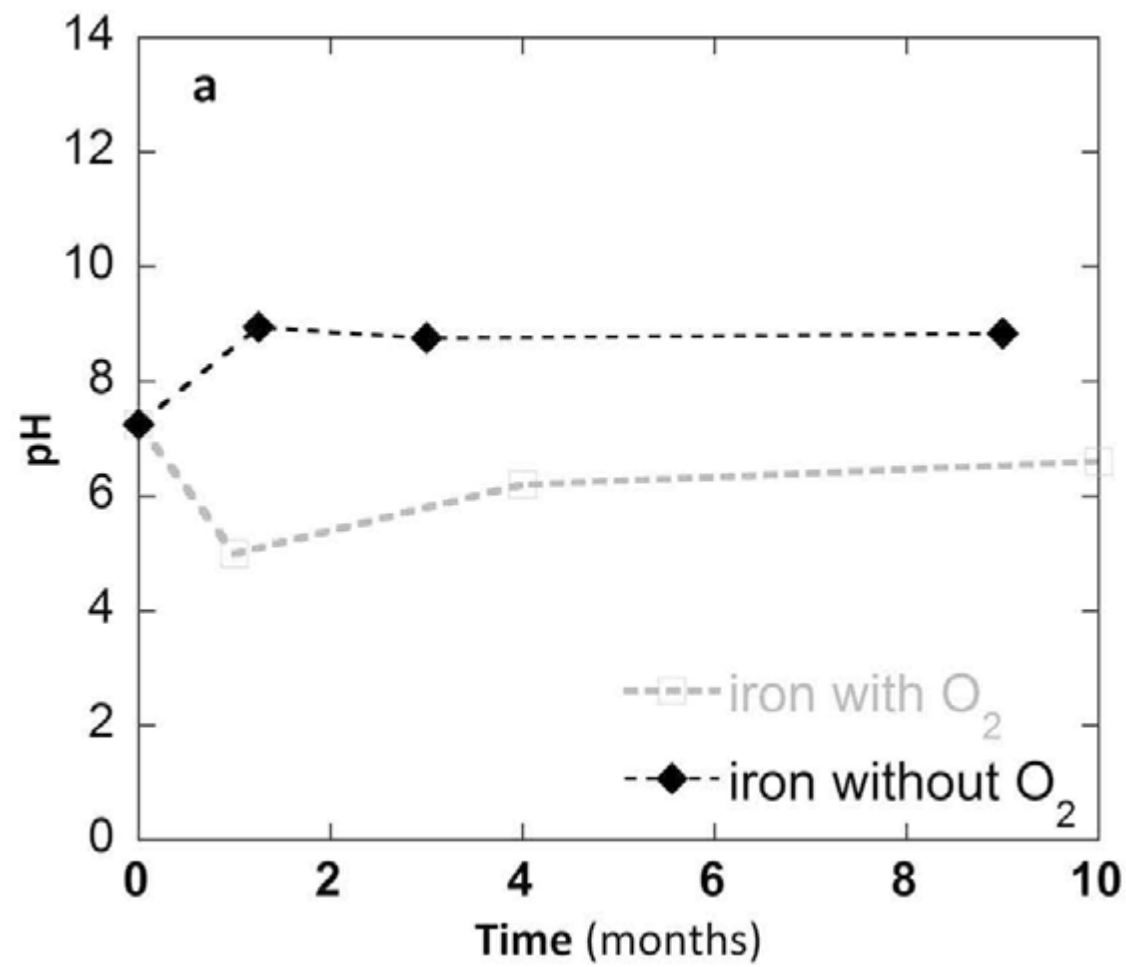
a
pH
Time (months)
iron with O2
iron without O2

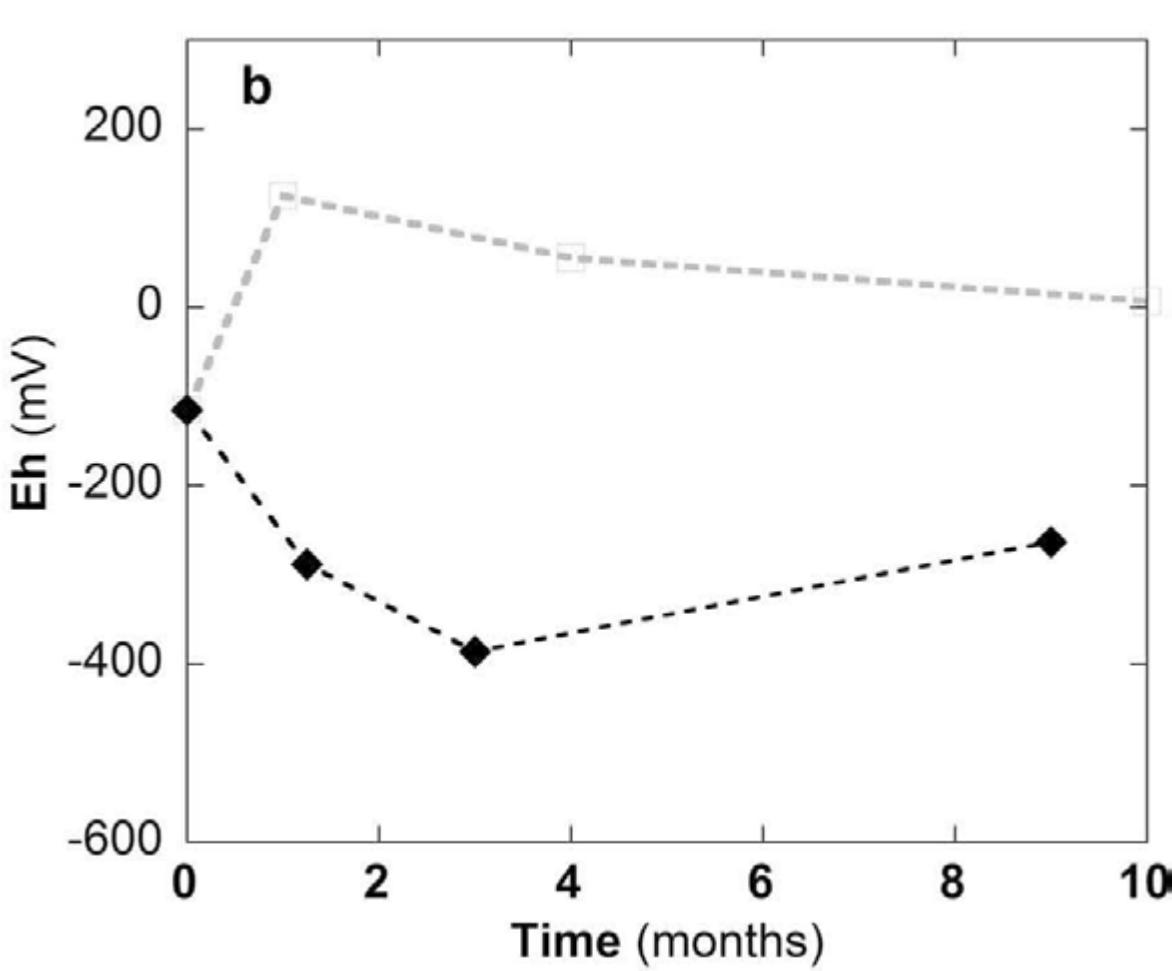
b
Eh (mV)
Time (months)

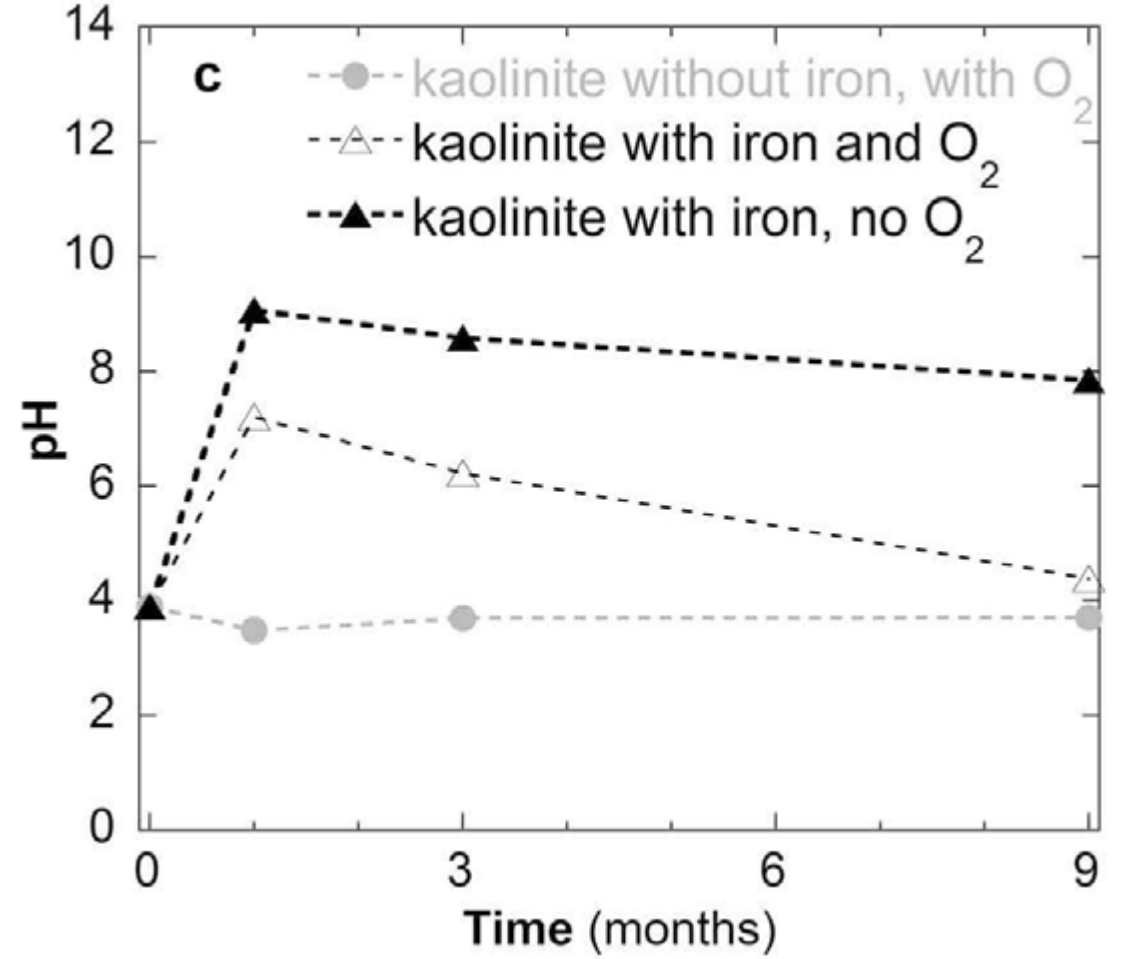
c
pH
Time (months)
kaolinite without iron, with O2
kaolinite with iron and O2
kaolinite with iron, no O2

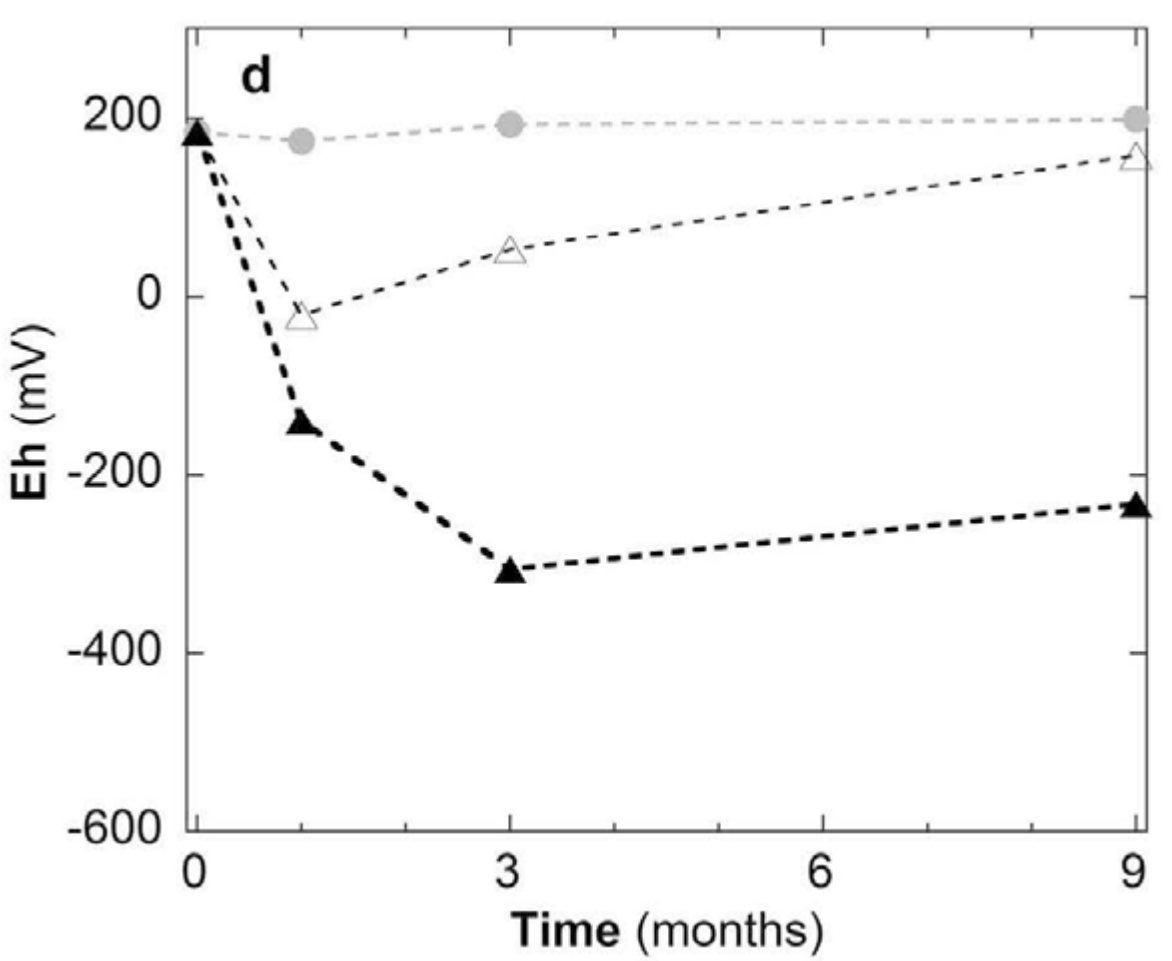
d
Eh (mV)
Time (months)

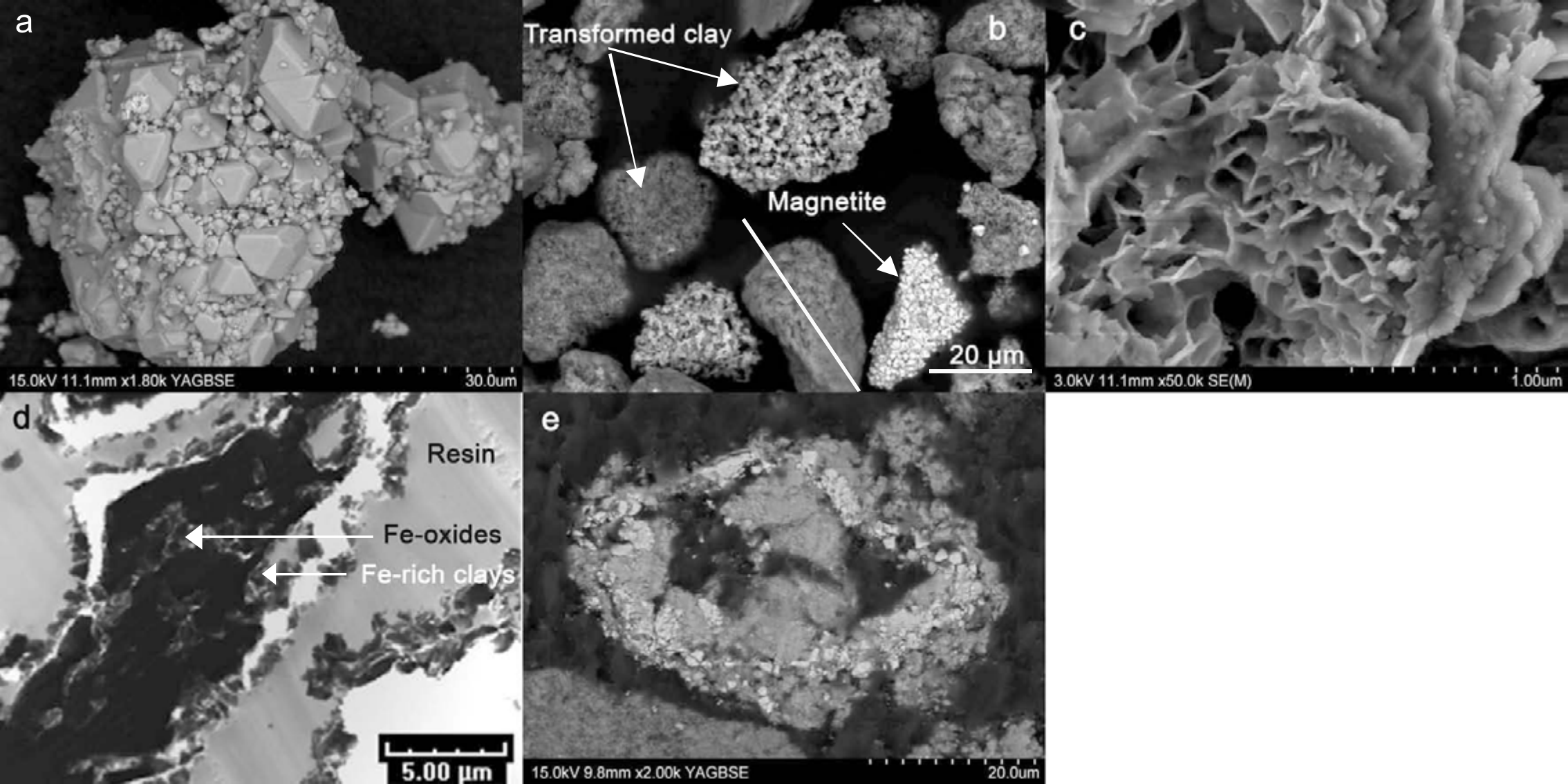
a
15.0kV 11.1mm x1.80k YAGBSE
30.0um
Transformed clay
b
Magnetite
20 µm
c
3.0kV 11.1mm x50.0k SE(M)
1.00um
d
Resin
Fe-oxides
Fe-rich clays
5.00 µm
e
15.0kV 9.8mm x2.00k YAGBSE
20.0um

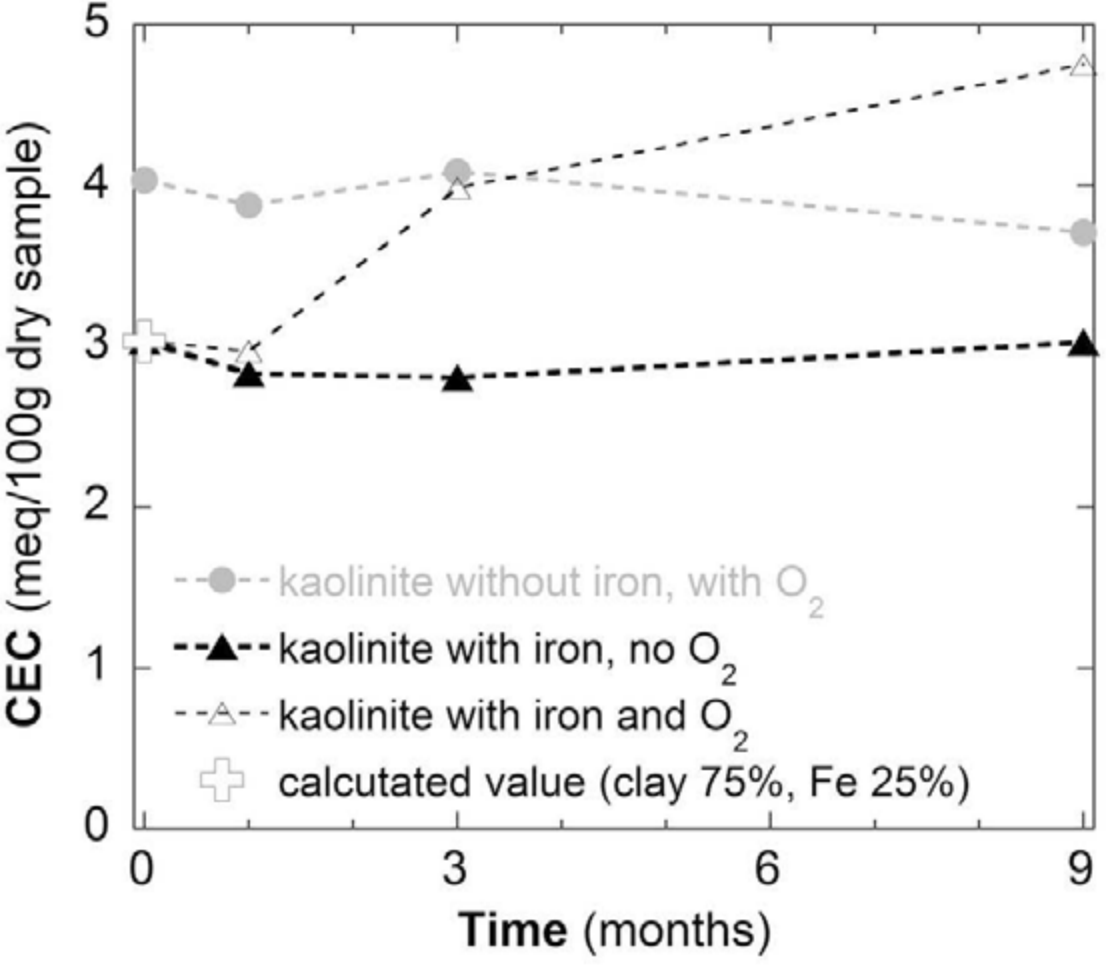
5
4
3
2
1
0
CEC (meq/100g dry sample)
0
3
6
9
Time (months)
kaolinite without iron, with O2
kaolinite with iron, no O2
kaolinite with iron and O2
calcutated value (clay 75%, Fe 25%)

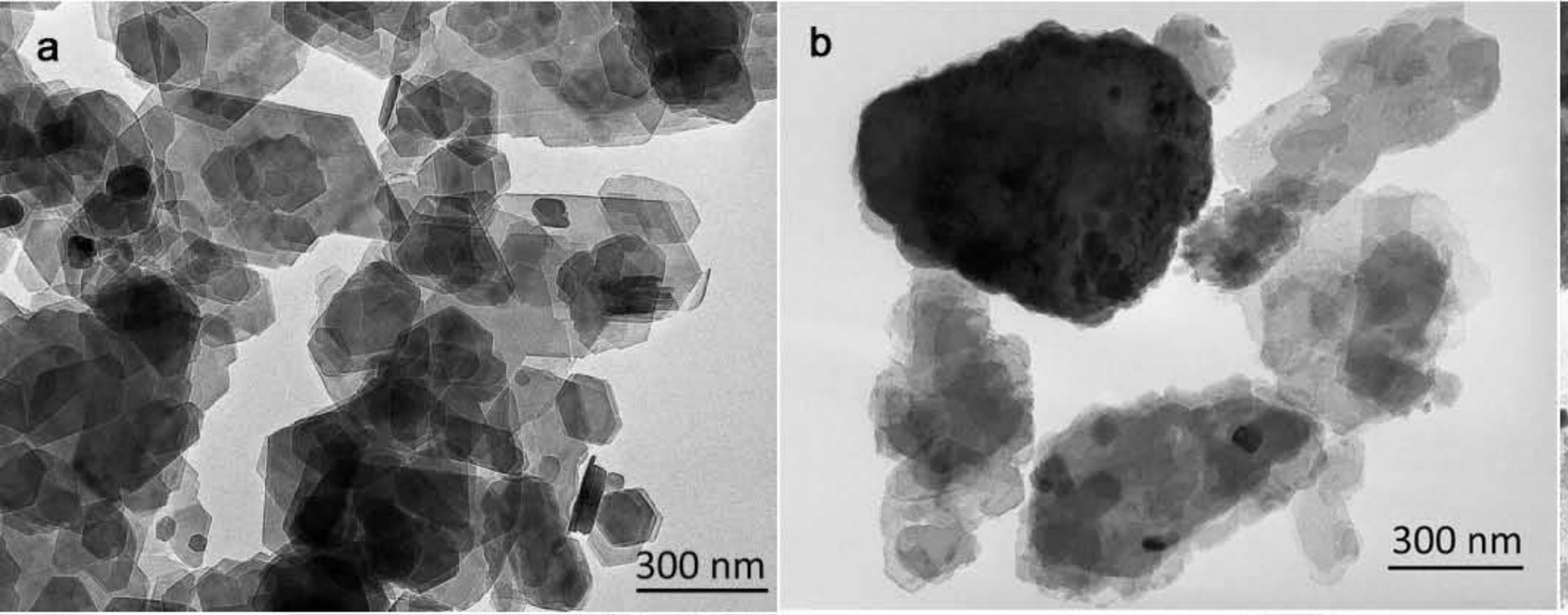
a
300 nm

b
300 nm

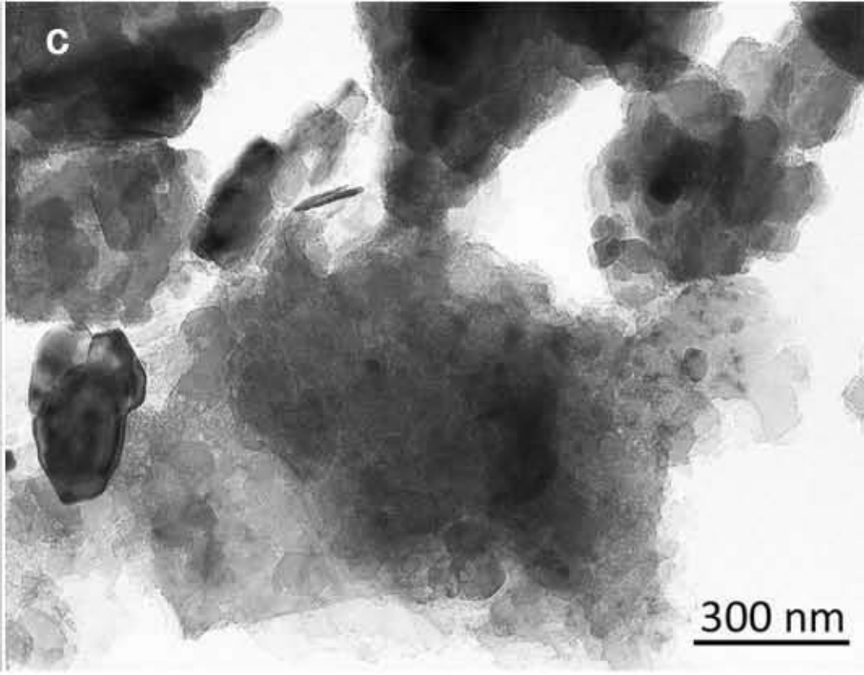
c
300 nm

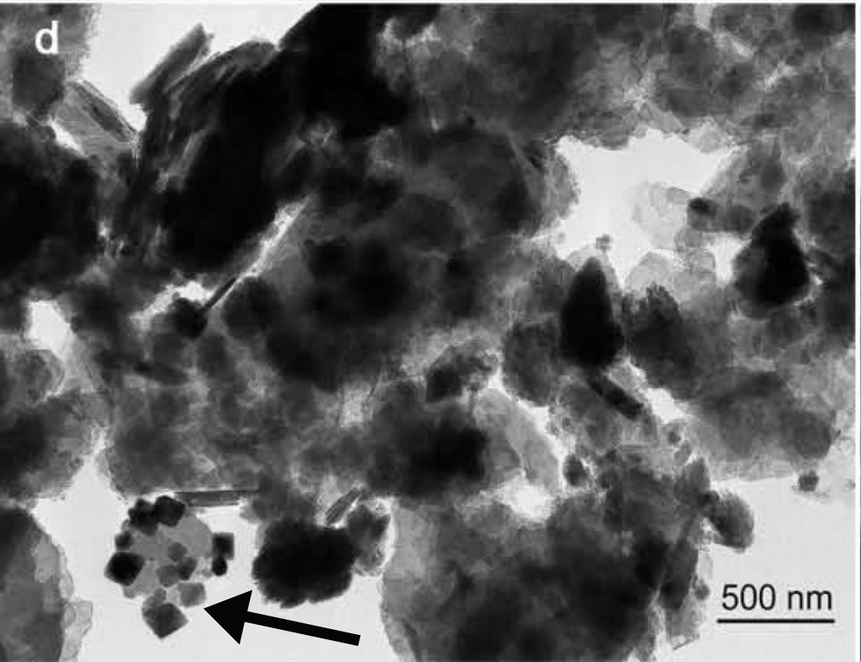
d
500 nm

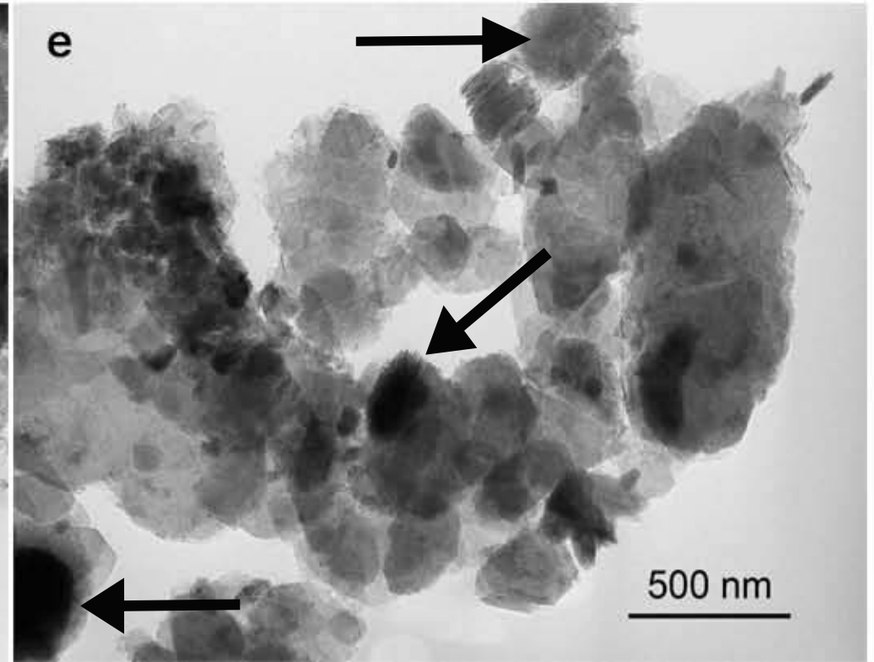
e
500 nm

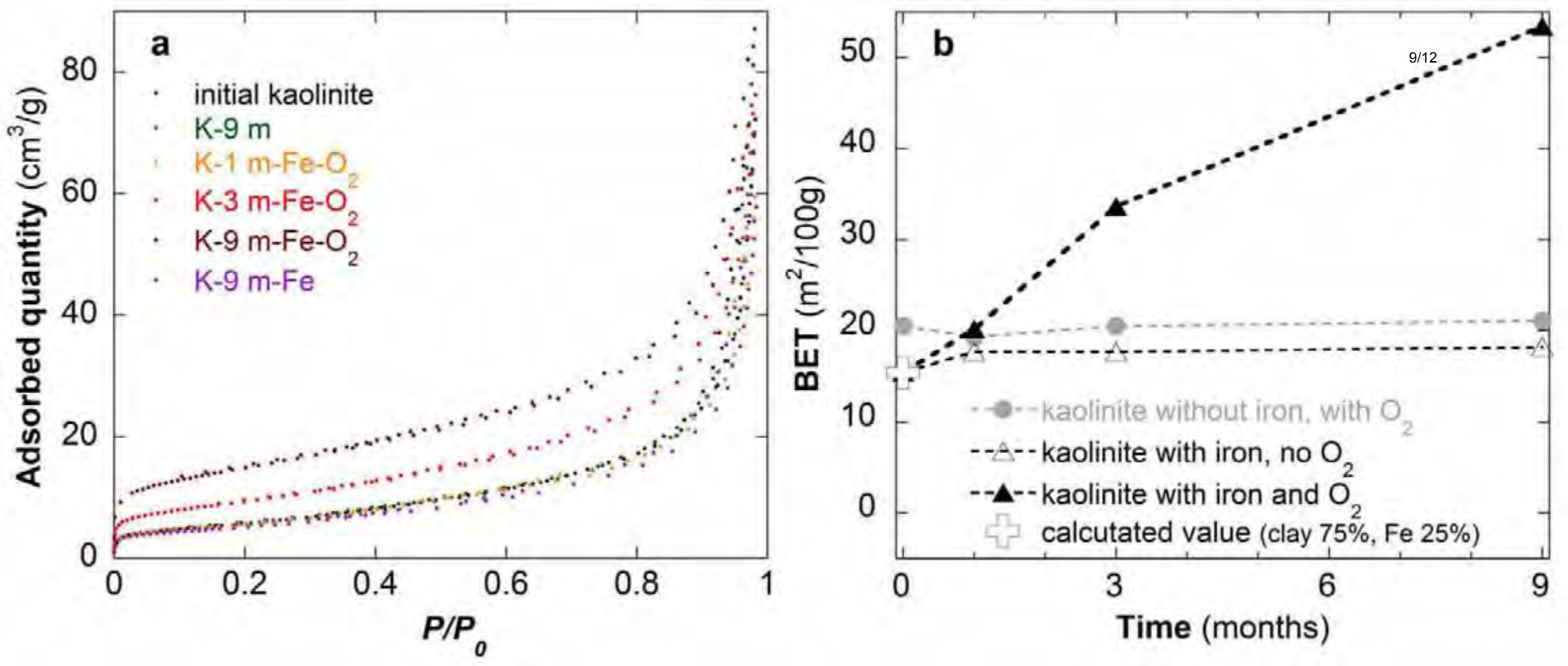
a
initial kaolinite
K-9 m
K-1 m-Fe-O2
K-3 m-Fe-O2
K-9 m-Fe-O2
K-9 m-Fe
Adsorbed quantity (cm3/g)
P/P0
0
20
40
60
80
0.2
0.4
0.6
0.8
1
b
BET (m2/100g)
Time (months)
kaolinite without iron, with O2
kaolinite with iron, no O2
kaolinite with iron and O2
calcutated value (clay 75%, Fe 25%)
10
30
50
3
6
9

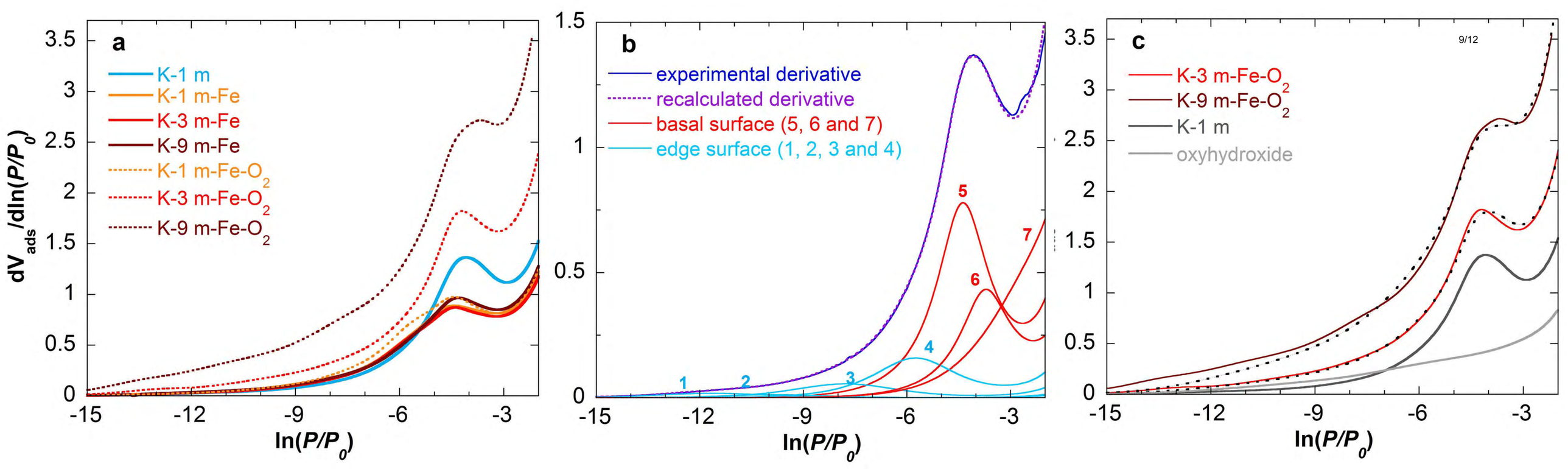
a
K-1 m
K-1 m-Fe
K-3 m-Fe
K-9 m-Fe
K-1 m-Fe-O2
K-3 m-Fe-O2
K-9 m-Fe-O2
dVads/dln(P/P0)
ln(P/P0)
b
experimental derivative
recalculated derivative
basal surface (5, 6 and 7)
edge surface (1, 2, 3 and 4)
1
2
3
4
5
6
7
ln(P/P0)
c
9/12
K-3 m-Fe-O2
K-9 m-Fe-O2
K-1 m
oxyhydroxide
ln(P/P0)

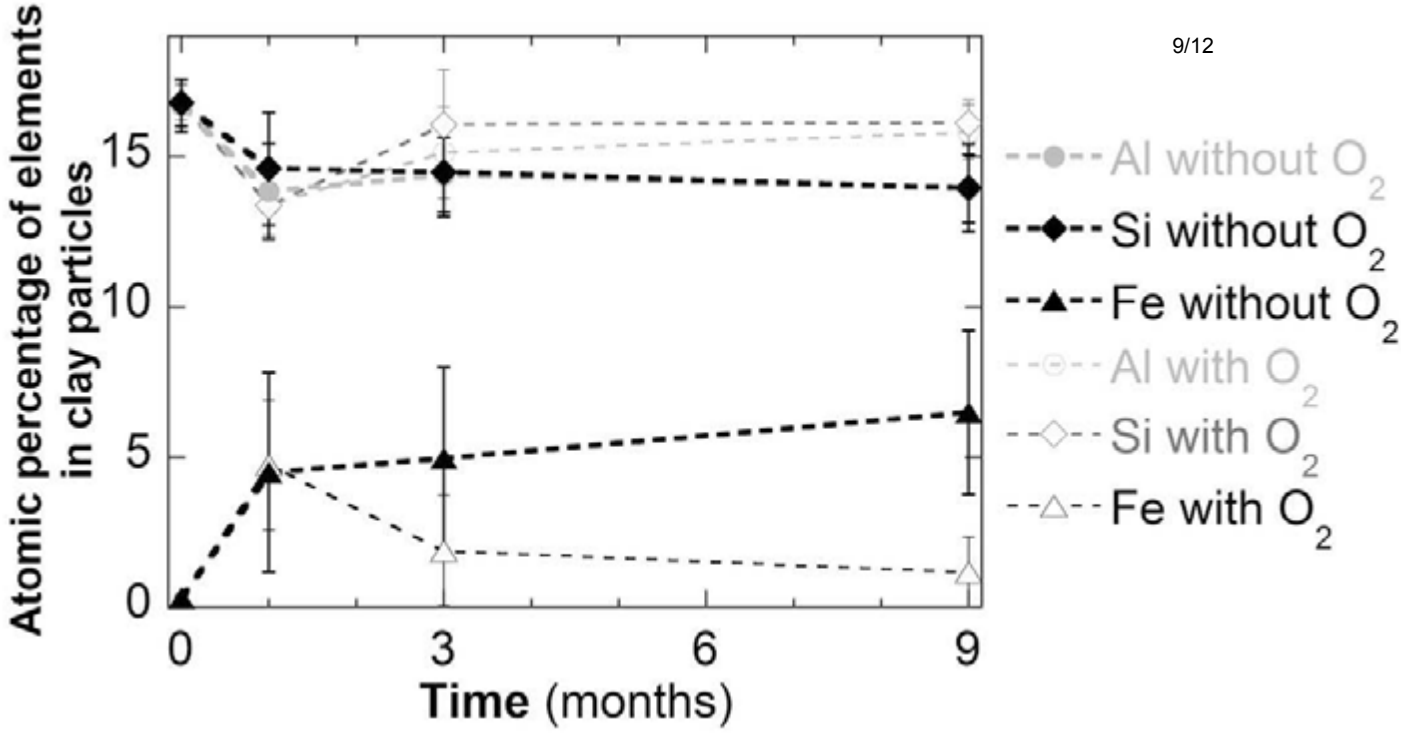
Atomic percentage of elements in clay particles
0
5
10
15
0
3
6
9
Time (months)
Al without O2
Si without O2
Fe without O2
Al with O2
Si with O2
Fe with O2

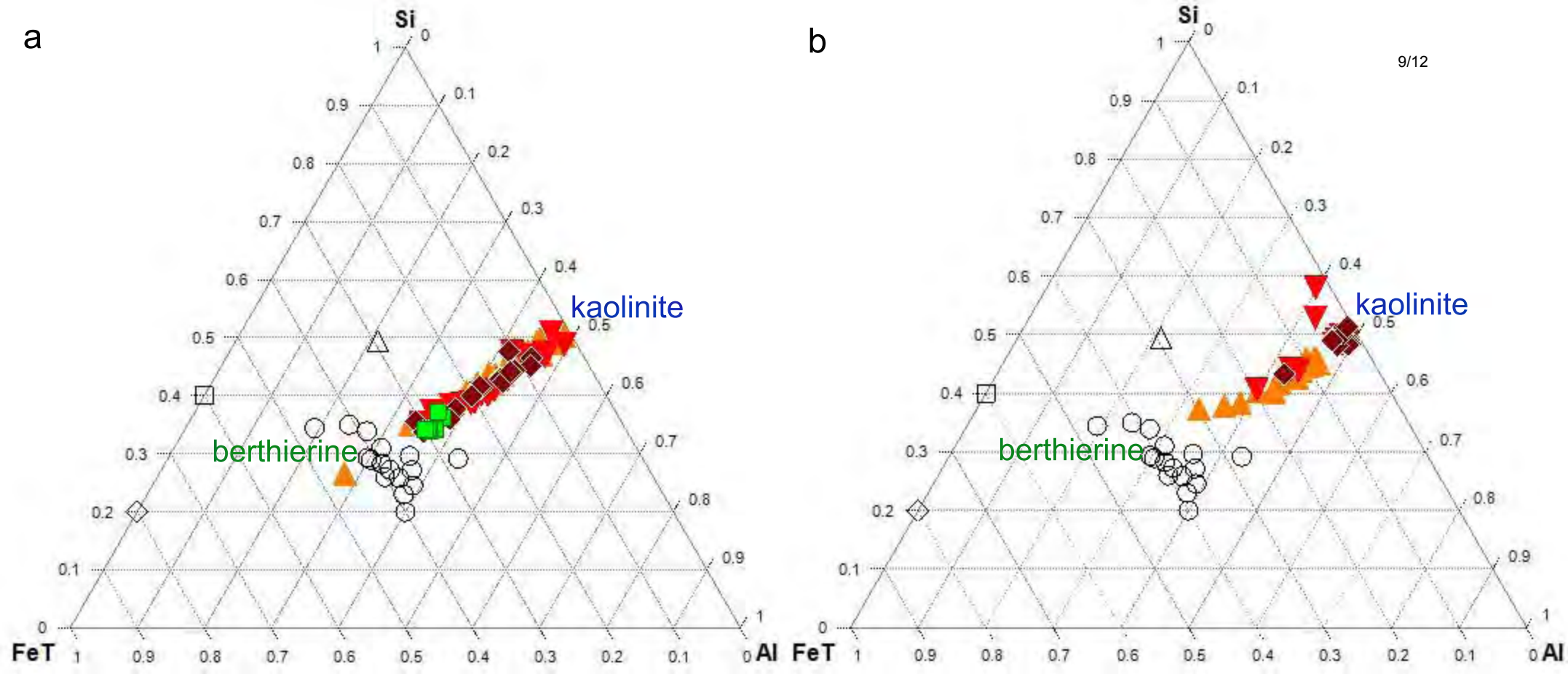
a
b
Si
FeT
Al
kaolinite
berthierine
9/12

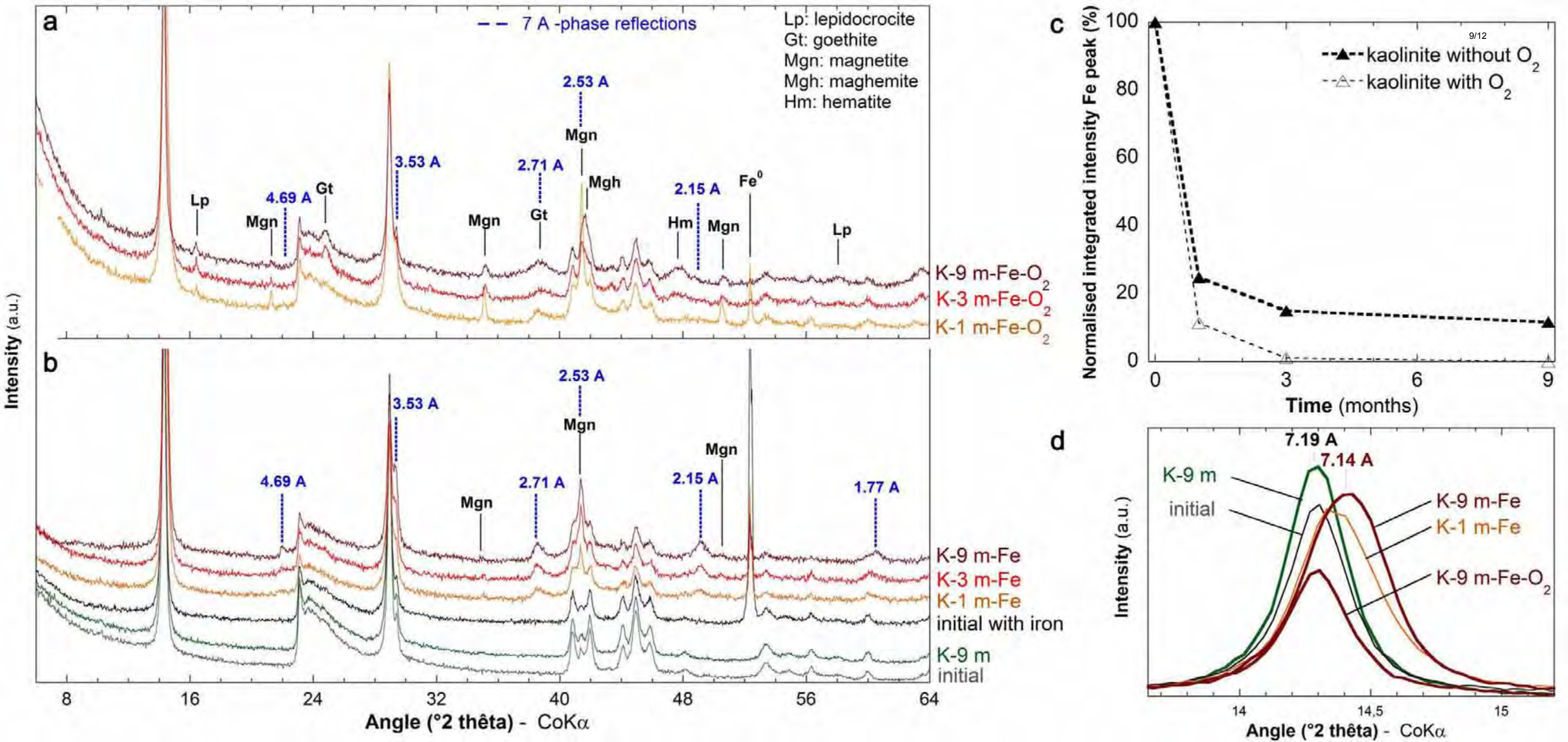
a
7 A -phase reflections
Lp: lepidocrocite
Gt: goethite
Mgn: magnetite
Mgh: maghemite
Hm: hematite
2.53 A
Mgn
3.53 A
2.71 A
Mgh
2.15 A
Fe0
4.69 A
Gt
Lp
Mgn
Gt
Hm
Mgn
Lp
K-9 m-Fe-O2
K-3 m-Fe-O2
K-1 m-Fe-O2
b
2.53 A
3.53 A
Mgn
4.69 A
2.71 A
2.15 A
Mgn
1.77 A
Mgn
K-9 m-Fe
K-3 m-Fe
K-1 m-Fe
initial with iron
K-9 m
initial
Intensity (a.u.)
8
16
24
32
40
48
56
64
Angle (°2 thêta) - CoKα
c
Normalised integrated intensity Fe peak (%)
100
80
60
40
20
0
kaolinite without O2
kaolinite with O2
0
3
6
9
Time (months)
d
7.19 A
7.14 A
K-9 m
initial
K-9 m-Fe
K-1 m-Fe
K-9 m-Fe-O2
Intensity (a.u.)
14
14,5
15
Angle (°2 thêta) - CoKα

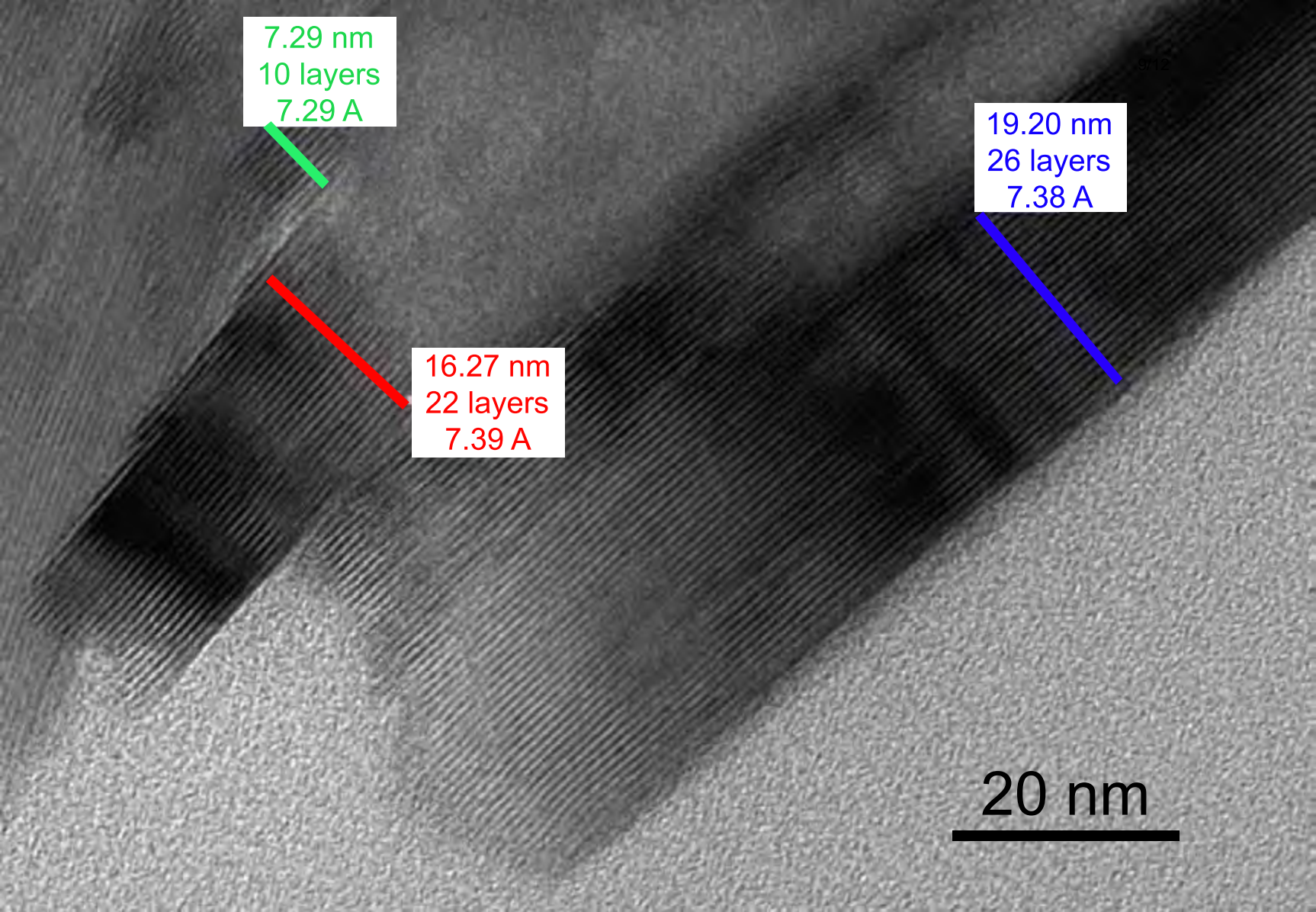
7.29 nm
10 layers
7.29 A
16.27 nm
22 layers
7.39 A
19.20 nm
26 layers
7.38 A
20 nm

a

SAED

200 nm

[001]

$\bar{3}30$

$\bar{2}20$

$\bar{1}10$

060

040

020

110

220

330

b

SAED

200 nm

[001]

$\bar{2}20$ k

$\bar{2}20$ b

010 b

020 k

030 b

060 k

220 b

220 k

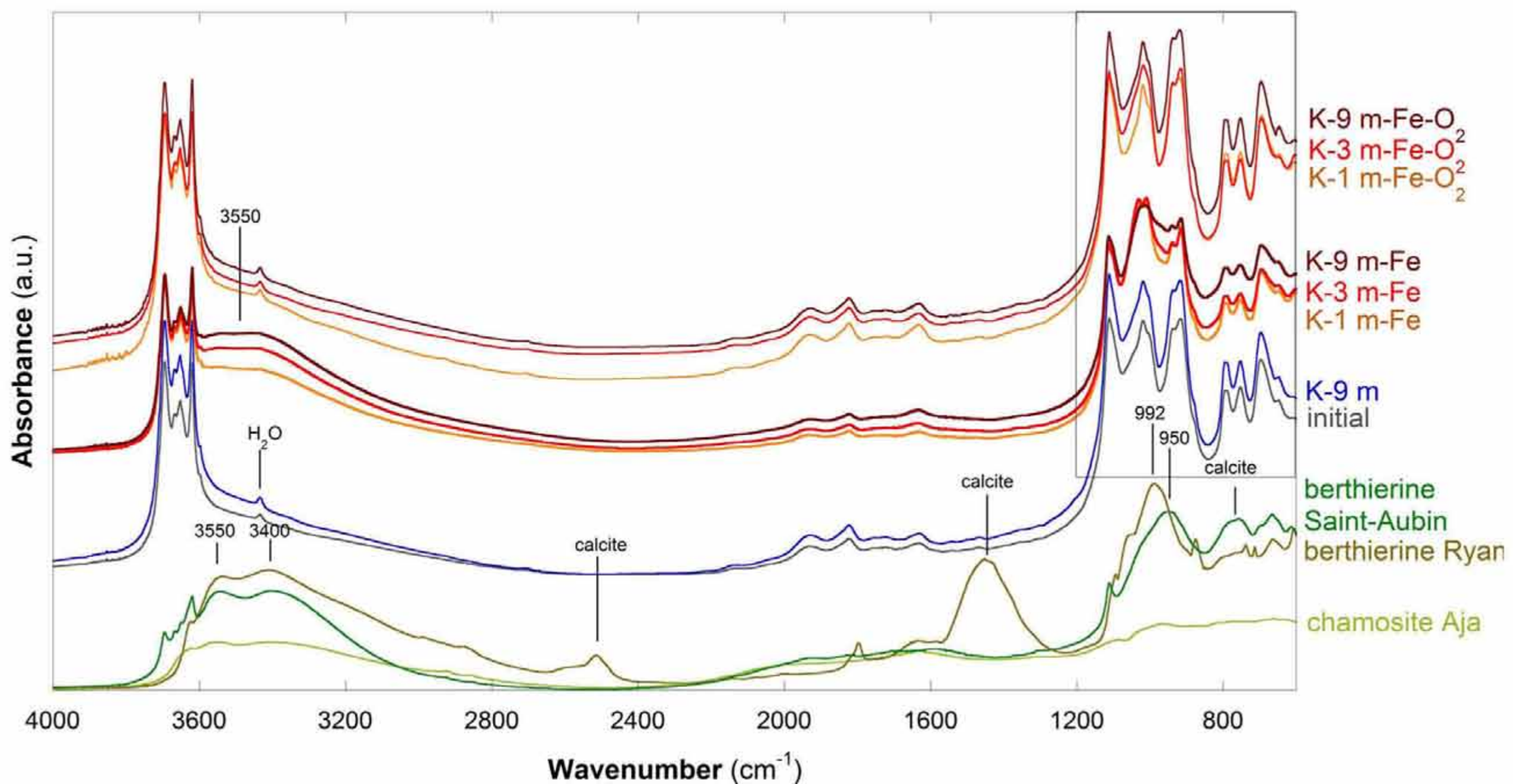
Absorbance (a.u.)
3550
H2O
3550
3400
calcite
calcite
992
950
calcite
K-9 m-Fe-O2
K-3 m-Fe-O2
K-1 m-Fe-O2
K-9 m-Fe
K-3 m-Fe
K-1 m-Fe
K-9 m
initial
berthierine
Saint-Aubin
berthierine Ryan
chamosite Aja
4000
3600
3200
2800
2400
2000
1600
1200
800
Wavenumber (cm-1)

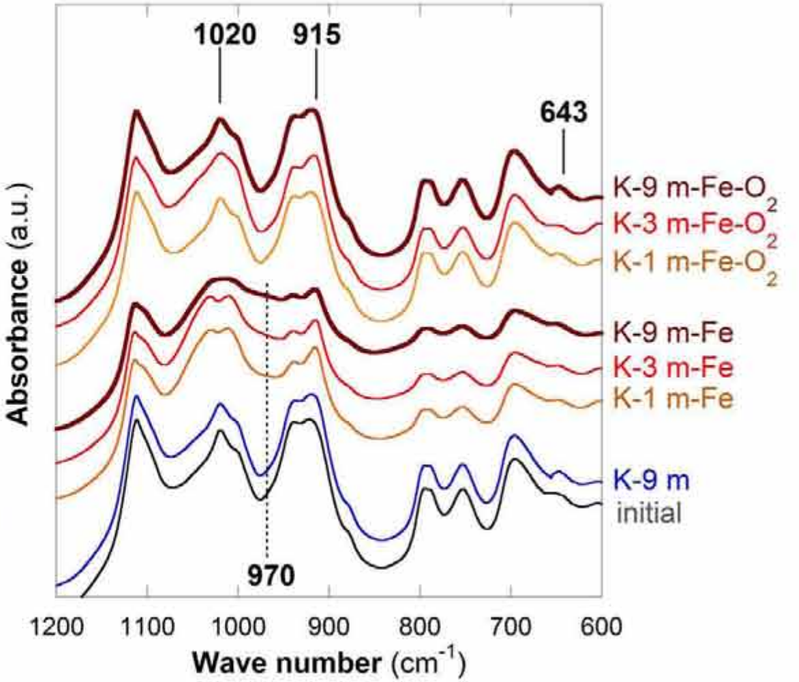
1020
915
643
970
Absorbance (a.u.)
K-9 m-Fe-O2
K-3 m-Fe-O2
K-1 m-Fe-O2
K-9 m-Fe
K-3 m-Fe
K-1 m-Fe
K-9 m
initial
1200
1100
1000
900
800
700
600
Wave number (cm-1)

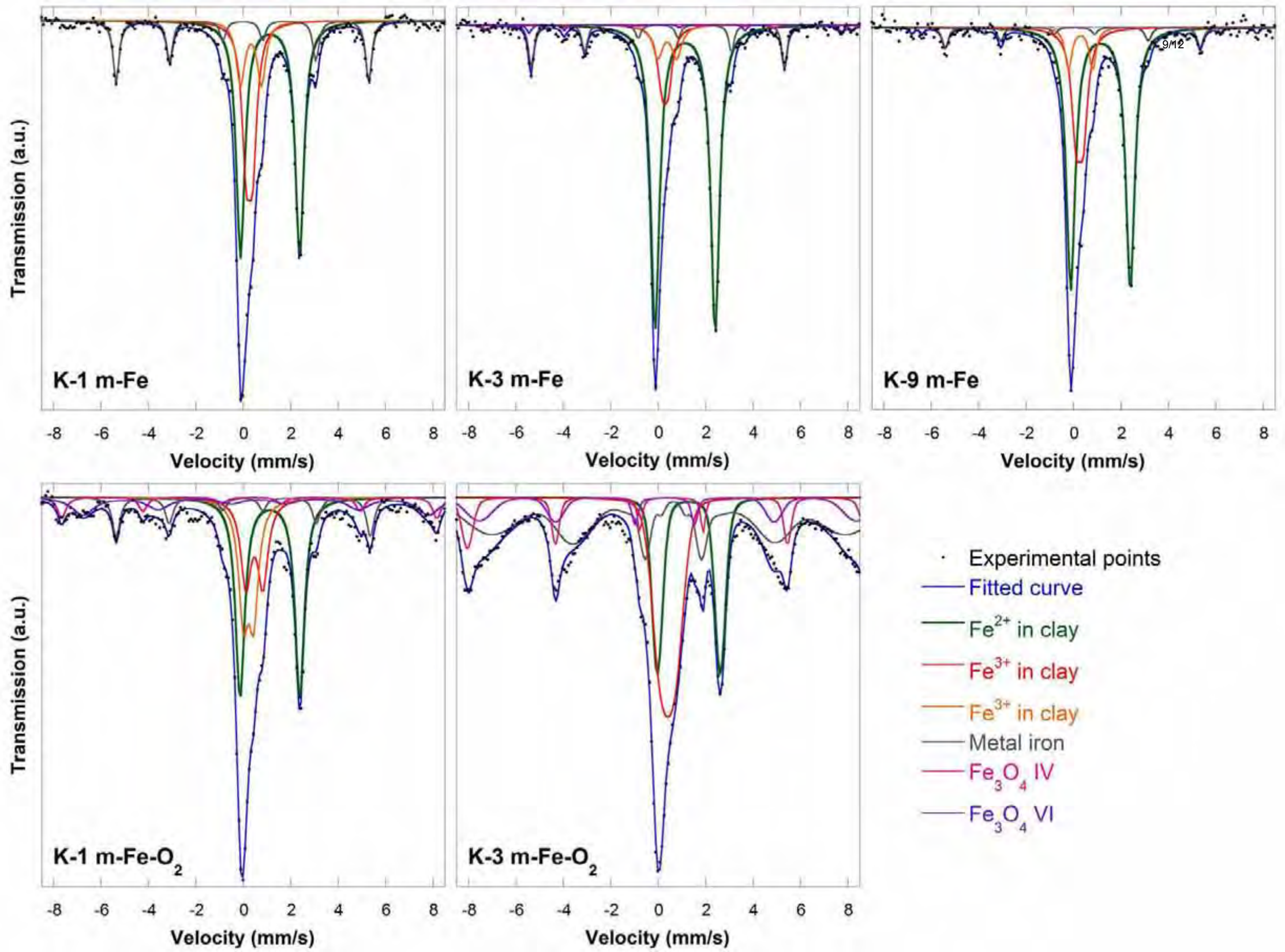
Transmission (a.u.)
K-1 m-Fe
K-3 m-Fe
K-9 m-Fe
K-1 m-Fe-O2
K-3 m-Fe-O2
-8 -6 -4 -2 0 2 4 6 8
Velocity (mm/s)
Experimental points
Fitted curve
Fe2+ in clay
Fe3+ in clay
Fe3+ in clay
Metal iron
Fe3O4 IV
Fe3O4 VI

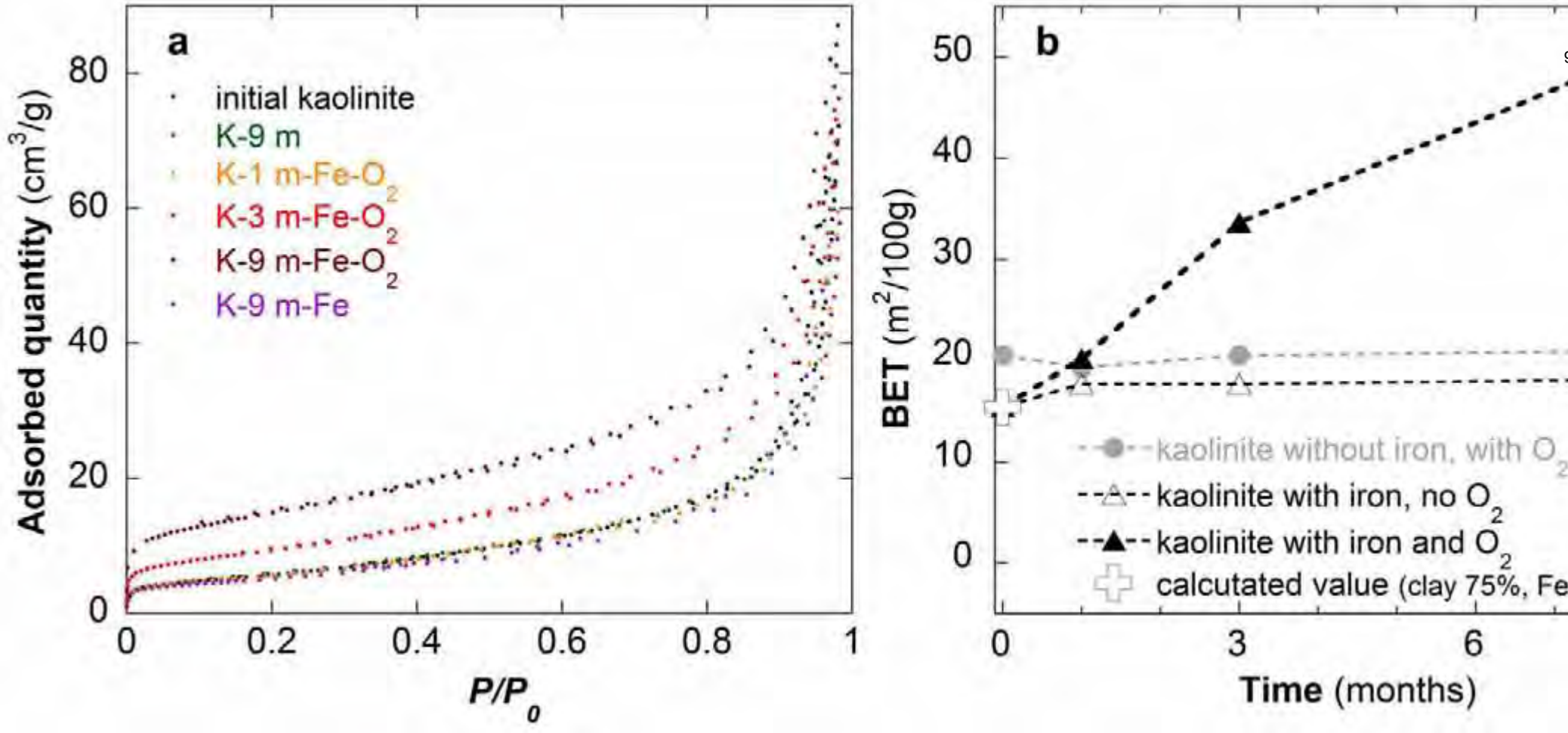
a
initial kaolinite
K-9 m
K-1 m-Fe-O2
K-3 m-Fe-O2
K-9 m-Fe-O2
K-9 m-Fe
Adsorbed quantity (cm3/g)
P/P0
0
20
40
60
80
0.2
0.4
0.6
0.8
1
b
BET (m2/100g)
Time (months)
kaolinite without iron, with O2
kaolinite with iron, no O2
kaolinite with iron and O2
calcutated value (clay 75%, Fe
0
10
20
30
40
50
3
6

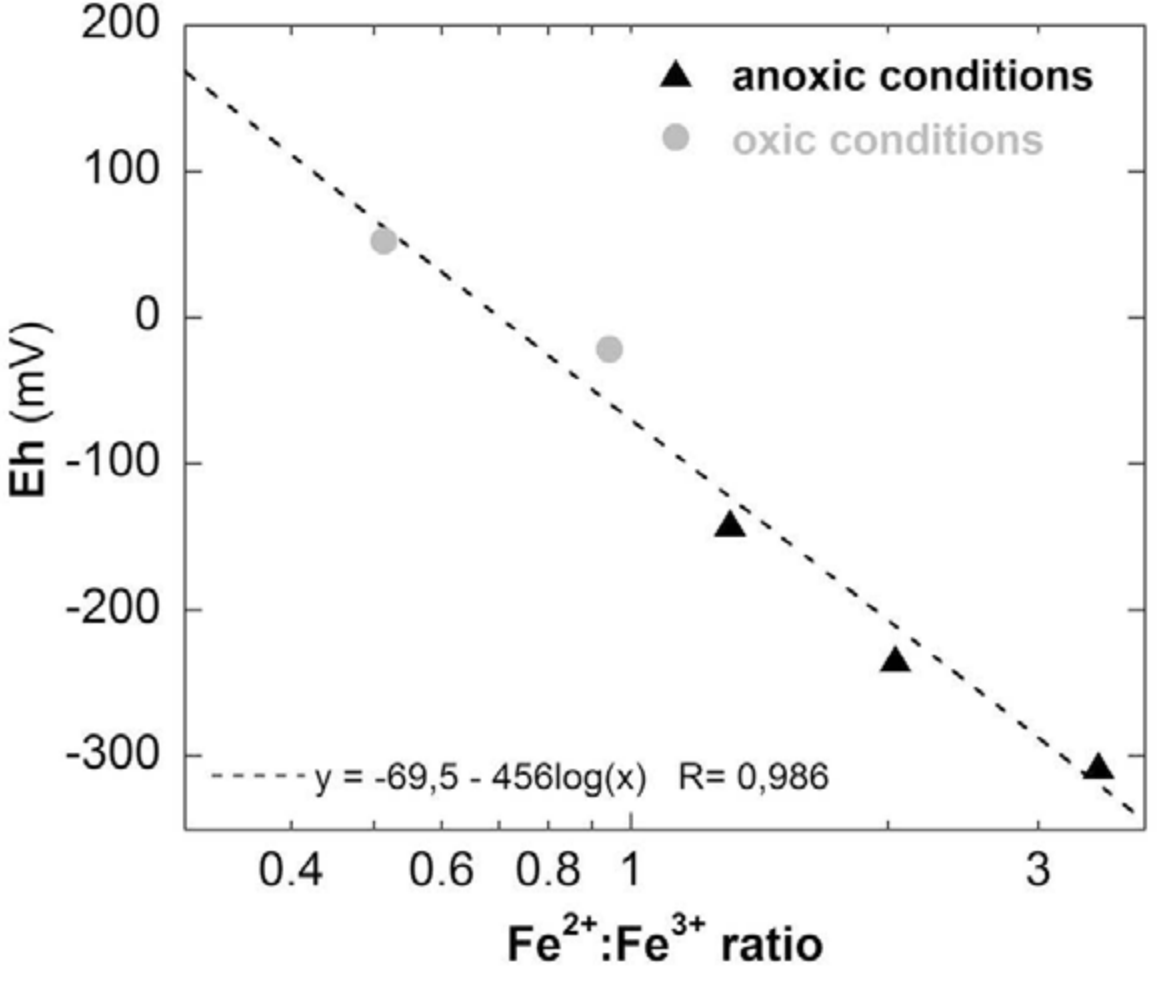
200
100
0
-100
-200
-300
Eh (mV)
anoxic conditions
oxic conditions
y = -69,5 - 456log(x) R= 0,986
0.4
0.6
0.8
1
3
Fe2+:Fe3+ ratio

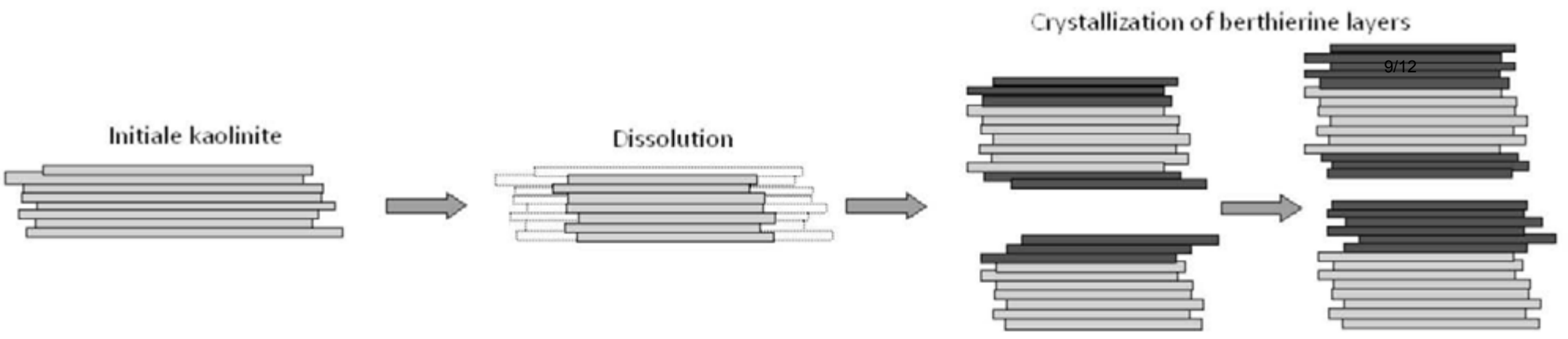
Initiale kaolinite
Dissolution
Crystallization of berthierine layers